Wave propagation models for numerical wave tanks

Eugeny Buldakov

UCL, Department of Civil Engineering, Gower Street, LONDON, WC1E 6BT, UK

Abstract

This chapter discusses the importance of efficient wave propagation models for generating boundary conditions for CFD models of wave-structure interaction or as elements of hybrid models. We give a brief review of fully nonlinear wave models based on potential flow theory (FNPT), which are the main candidates for such applications. We then suggest a Lagrangian wave model as an alternative to classical FNPT models. We present a mathematical and numerical formulation of the model, its validation and application to propagation of steep wave groups and to wave groups on sheared currents.

1. Introduction

Most wave-structure interaction models are based on a numerical solution of boundary value problems for partial differential equations. For such models the solution accuracy depends not only on the quality of the numerical approximation of the equations, but also on the accuracy of the boundary conditions. Apart from defining the physical boundaries of a fluid domain, they are used to specify the incoming wave conditions. A common numerical tool for modelling wave-structure interaction is a numerical wave tank (NWT), where the fluid domain is bounded and waves are generated by a numerical wavemaker, e.g. by specifying wave kinematics and elevation at the incoming boundary. Difficulties experienced by NWT users are very similar to difficulties of wave generation in experimental wave facilities. These include the accuracy of incoming wave generation and reflections from the boundaries of the fluid domain.

Effective absorption of reflected waves normally requires large absorbing zones and thus larger computational domains. At the same time, a sufficient distance from the wavemaker to the test section is recommended to allow the natural development of the waves. Depending on the absorption method and

type of a wavemaker, this can lead to a considerable increase in the size of the NWT. On the other hand, to achieve higher computational efficiency, it is necessary to minimise the size of the computational domain around a structure. This is particularly important because of the high demands of modern computational fluid dynamics (CFD) models for computing resources. Furthermore, for the direct comparison between experiments and calculations and for the execution of computer-assisted experiments, it is useful to model an entire experimental wave tank with the exact replication of the wavemaker shape and the position of the model. This again leads to a much larger domain size than the region of interest around the structure. Often, the optimal NWT size for accurate wave input is impractical for CFD models in terms of computational efficiency. As can be seen, a numerical wave-structure interaction model should satisfy conflicting requirements and it would be natural to apply different models in different regions of a computational domain or to simulate different aspects of the process. For example, a simpler and faster model can be used to simulate wave evolution in the far field, and the region close to the structure can be modelled by a more sophisticated, but slower, CFD model.

The idea of hybrid models recently received considerable attention and numerous hybrid models have been developed. The most popular couple for creating a hybrid model are a boundary element model (BEM) as a computationally efficient component and volume of fluid (VoF) as an advanced component (e.g. Lachaume et al., 2003; Kim et al., 2010; Guo et al., 2012). However, coupling of other models has also been attempted, for example BEM with SPH (Landrini et al., 2012) and a finite element method (FEM) with a meshless Navier-Stokes solver (Sriram et al., 2014). More examples can be found in the introduction to Sriram et al. (2014). The hybrid methods revive simple but computationally efficient wave propagation models as important elements of wave-structure interaction modelling tools. Over the years, many numerical models of nonlinear water waves have been developed. Descriptions of numerical methods for water wave modelling and reviews of numerical simulation of water waves can be found in Tsai and Yue (1996); Fenton (1999); Kim et al. (1999); Dias and Bridges (2006); Lin (2008); Ma (2010).

In this chapter we consider inviscid models and we start with a brief historical review of models based on the fully nonlinear potential flow theory (FNPT) given in Section 2. In comparison with CFD models, based on solving Reynolds Averaged Navier-Stokes equations, these methods use

much simpler governing equations with smaller number of variables. As a result, FNPT models are more efficient computationally. At the same time, they are able to reproduce the principal physical phenomena important for wave propagation, namely non-linearity and dispersion. As a result, such models describe propagation of highly nonlinear waves up to breaking with good accuracy, as demonstrated by multiple comparisons with experiments (e.g. Dommermuth et al., 1988; Skyner, 1996; Seiffert et al., 2017). We will not consider models based on further simplifications, such as depth-averaged models (shallow water and Boussinesq equations) or models of spectral evolution (nonlinear Schrödinger equation, Zakharov equation). Since we consider the wave propagation problem, we will not review literature related to application of FNPT models to interaction with structures, floating bodies, etc.

FNPT models differ by particular methods of solving Laplace equation for velocity potential in the fluid domain and by methods of specifying a fully nonlinear boundary condition on a moving free surface. There are three main classes of numerical methods used to solve wave problems in potential formulation: boundary element methods (BEM), finite element methods (FEM) and high-order spectral methods (HOS). They are discussed in separate parts of Section 2. We do not consider various finite difference methods, which use a wide range of approaches to discretise a moving domain, including boundary-fitted coordinates and σ-transform. They can not be considered the mainstream for inviscid models and an interested reader is referred to the reviews of Tsai and Yue (1996); Fenton (1999) and Kim et al. (1999). Section 2 concludes with a brief review of Lagrangian wave models, which offer certain advantages and can be considered as an alternative to conventional FNPT models.

The rest of the chapter discusses a wave propagation model based on Lagrangian description of fluid motion and is organised as follows. Section 3 gives a detailed description of the Lagrangian wave model. The section presents the mathematical and numerical formulation of the model. Then, it introduces a method of numerical treatment of breaking waves, discusses the computational efficiency of the model and validates the model with experimental results. In Section 4 the model is applied to evolution of steep breaking wave groups in a wave flume. In Section 5 the model formulation for waves over sheared currents is introduced and a numerical wave-current flume is constructed and applied to simulate wave groups over following and opposing currents. Both Section 4 and 5 include a comparison between ex-

perimental and numerical results. Finally, brief concluding remarks are given in Section 6, where model coupling for wave-structure interaction problems is discussed.

2. Historical development

2.1. BEM models

Boundary element methods can be traced back to the work of Longuet-Higgins and Cokelet (1976) who considered the evolution of two-dimension space-periodic waves in deep water. They work in complex variables and use conformal mapping to transform a semi-infinite periodic domain into internals of a closed contour representing the mapped free surface. The material time derivatives of surface coordinates and of surface potential are then expressed via the normal derivative of the potential. To find the normal derivative the Dirichlet problem of finding the normal gradient of a harmonic function from its values on a closed contour is formulated and solved by using Green's theorem. This leads to an integral equation relating the normal gradient of the potential with its values at the mapped free surface. The integral equation is solved numerically and the normal derivative of the potential is used to calculate the time derivatives. Then material coordinates of the free surface and the surface potential at the incremented time are calculated by using a fourth-order finite difference technique. The numerical scheme demonstrated a week saw-toothed instability which was suppressed by applying polynomial smoothing. The method was applied to simulate the evolution of high periodic waves and development of overturning profiles at initial stages of wave breaking. Since the method uses the Lagrangian approach to track the evolution of the free surface, it is referred to as a mixed Eulerian-Lagrangian method (MEL). This becomes a common feature of boundary-element methods. Later, the method was extended to the case of constant finite depth (New et al., 1985). Vinje and Brevig (1981) suggested an alternative method where Cauchy's integral theorem is applied to a complex flow potential in physical space. Working in physical variables allowed to construct solutions with vertical solid boundaries (fixed or moving) and to simulate waves in a wave flume with a piston wavemaker (Dommermuth et al., 1988).

Using complex variables restricts the application of the boundary integral formulation to 2D problems. A more flexible formulation was therefore developed with Green's theorem applied in physical space. Apart from being

applicable to both 2D and 3D problems, such formulation also allows flexible treatment of fixed and moving solid boundaries of arbitrary shape and is suitable for development of efficient numerical wave tanks. Examples of BEM-based 2D numerical wave tanks, which differ by details of numerical realisation and methods of wave generation and absorption can be found in Grilli et al. (1989); Ohyama and Nadaoka (1991); Wang et al. (1995). Though the first works on application of BEM to 3D waves appeared relatively early (e.g Isaacson, 1982), it took long time to develop robust and flexible models suitable for wide range of applications. Apart from the more difficult formulation for 3D geometry, this was caused by the drastic increase of computational cost for such models. Simplified formulations were often suggested to deal with these problems, which restricted models applicability. For example, Isaacson (1982) used a Green function that assumes the symmetry of the solution about the flat sea bed (method of images). This restricts the application of the method to constant depth. Xue et al. (2001) considered deep water waves periodic in both horizontal directions. This simplification allowed to perform high-resolution simulations and to obtain valuable results on dynamics and evolution of 3D breaking waves. Considerable efforts have finally resulted in the development of 3D numerical wave tanks capable of simulating general highly nonlinear waves on arbitrary bathymetry Grilli et al. (2001).

The solution method used by the models mentioned above and in fact by most contemporary BEM models can be briefly summarised as follows. By applying Green's theorem with an appropriate selection of the Green function, the Laplace equation can be reduced to an integral equation defined on a boundary of the computational domain. The equation relates the values of the potential and its normal derivative at the boundary. The free surface boundary conditions are written in the mixed Eulerian-Lagrangian form and connect the material time derivatives of the surface potential and of the surface position with the gradient of the potential (velocity) at the free surface. If both the potential and the normal derivative are known, the time derivatives can be calculated. The boundary conditions on solid surfaces specify the normal derivatives of the potential at these boundaries (Neumann boundary condition). For the free surface, the surface potential is known either from the initial conditions or from a previous calculation step (Cauchy boundary condition). Then, the boundary integral equation can be used to calculate the normal derivatives at the free surface and the potential at the solid boundary. After discretisation of the integral equation, a sys-

tem of linear algebraic equations is solved to find the unknown values of the potential and the normal derivative at the surface nodes. The free surface boundary conditions can then be used to update the free surface position and the surface potential by applying an appropriate time stepping technique.

Major improvements had been made in terms of the method accuracy and stability (e.g. Grilli and Svendsen, 1990). More recently, considerable efforts are concentrated on improving computational efficiency of BEM models (Fochesato and Dias, 2006; Yan and Liu, 2011; Jiang et al., 2012) and to the adaptation of the method for parallel computing (Nimmala et al., 2013). Over the years BEM models have been applied to a wide range of water wave problems including problems of propagation of extreme waves directly relevant to this chapter (e.g. Fochesato et al., 2007; Ning et al., 2009). For further reference, the up-to-date formulation for a 3D BEM numerical wave tank with a review of earlier work and examples of applications can be found in Grilli et al. (2010).

2.2. FEM models

Finite Element Methods (FEM) are extensively used for a wide variety of fluid mechanics problems (e.g. Zienkiewicz et al., 2005). They are more universal than BEM and can be applied to solving nonlinear equations in domains of complex shapes using unstructured meshes. Realisation of a numerical wave tank by FEM within the FNPT approach seems relatively straightforward by the discretisation of a bounded fluids domain with Neumann boundary conditions on solid boundaries. The first known FEM model for nonlinear waves represents a fully developed 2D numerical wave tank (Wu and Eatock Taylor, 1994).

Most FEM implementations for water waves treat the moving surface using the MEL approach described above for BEM models. A typical FEM solution for a water wave problem includes the following steps. The free surface boundary conditions are represented in the mixed Eulerian-Lagrangian form, as previously described. The velocity potential in the computational domain is known from the initial conditions or from the previous step of the solution. The velocity at the free surface can then be recovered and the free surface conditions can be used to update the position of the free surface and the value of the surface potential using a suitable time stepping technique. This leads to the formulation of a mixed boundary value problem for the Laplace equation at the next time step with the Cauchy boundary conditions on the free surface and the Neumann boundary conditions on fixed or

moving solid surfaces. The boundary value problem is then solved using a finite element approach, e.g. the Galerkin method. This approach was successfully applied for constructing both 2D (Wu and Eatock Taylor, 1994) and 3D (Ma et al., 2001; Wu and Hu, 2004) numerical wave tanks.

The FEM formulation requires the discretisation of the entire fluid domain. This leads to a much larger number of unknowns compared to BEM, where only the domain boundary is discretised. However, the discretisation for BEM is based on surface integrals, which leads to linear systems with dense non-symmetric matrices On the other hand, FEM discretisation procedure leads to sparse linear systems because of the local nature of discrete differential operators, which include only a few spatially close nodes. As a result, the number of non-zero matrix elements for FEM is much smaller. In addition, for regular meshes, the resulting matrix has a diagonal structure. If a typical number of discrete elements in one of the spatial dimensions is N, then for a 3D problem the number of nodes for FEM is $\sim N^3$ and for BEM it is $\sim N^2$. The corresponding numbers of matrix elements are $\sim N^6$ and $\sim N^4$ and the number of non-zero elements being receptively $\sim N^3$ and $\sim N^4$. This implies higher computational efficiency of FEM compared to BEM. Wu and Eatock Taylor (1995) compared BEM and FEM models for a 2D wave problem and reported that in many cases the finite element method may be more efficient but admitted that this conclusion is based on limited experience. A discussion of numerical efficiency of FEM in comparison to BEM can also be found in Cai et al. (1998). Complementary advantages of BEM discretisation of moving domains near bodies and higher efficiency of FEM far from the body were used in coupled BEM-FEM models by Wu and Eatock Taylor (2003) in 2D and by Eatock Taylor et al. (2008) in 3D.

Although FEM models rely on the MEL formulation for updating the free surface, the difficulties in generating a computational mesh in highly deformed domains did not allow the application of early FEM models to overturning waves. Another serious disadvantage of these models is that the generation of an unstructured mesh is required at each time step. The repeated generation of such a mesh considerably increases the computational time. To overcome this difficulty, a moving mesh method was developed by Ma and Yan (2006). In this method the mesh is generated only once. After that, the mesh is deformed at each step with a simple algorithm. The original idea of mobile mesh came from the arbitrary Lagrangian-Eulerian (ALE) formulation for Navier-Stokes equations. However, a different mesh deformation algorithm is used, which does not use fluid velocities to move

mesh nodes. The method is therefore called the quasi-arbitrary Lagrangian-Eulerian finite element method (QALE-FEM). The new positions of the free surface nodes are found by following the surface particles and then relocating the nodes. Relocation distributes the nodes more evenly over the free surface and does not allow them to move too close or too far apart. Then, the positions of the internal nodes are calculated using the spring analogy method. Further development of the QALE-FEM model allowed simulating overturning waves (Yan and Ma, 2010).

There is ongoing work on improving numerical implementations of FEM for water wave models to achieve better accuracy, stability, and computational efficiency. This, for example, includes using different types of a finite element method, for example the method of spectral elements (Robertson and Sherwin, 1999; Engsig-Karup et al., 2016). The reader can find details of FEM water wave formulation and application examples in Ma and Yan (2010) and Wang and Wu (2011).

2.3. Spectral models

High-order spectral methods are undeniably the most computationally efficient methods for modelling nonlinear waves, being capable of simulating 3D random sea states at linear scales of tens of wavelengths during tens of wave periods (Ducrozet et al., 2007).

In an early application of a spectral method, Fenton and Rienecker (1982) represented the potential and surface elevation in a 2D periodic domain of constant depth via Fourier expansion by basic functions satisfying the Laplace equation and boundary conditions. If the initial values of the Fourier coefficients are known, the kinematic free-surface condition can be used to advance the surface elevation using a finite difference approximation of the time derivative. All spatial derivatives are computed in the Fourier space. Inverse Fourier transforms are then used to perform a time step in the physical space. This simple approach, however, can not be applied to advance the potential. Instead, the dynamic free surface condition is used to calculate the time derivatives of each Fourier coefficient, which are then used to find the values of the coefficients at the next time step. Calculating derivatives requires solving a large system of simultaneous equations, which is responsible for the low computational efficiency of the method.

This problem was solved in high-order spectral methods (Dommermuth and Yue, 1987a; West et al., 1987). In this method, the potential is expressed as an asymptotic expansion by a small parameter. In addition, the free

surface potential is expanded in a Taylor series around the mean water level, and a double expansion is used to represent the surface potential. The known initial values of surface potential and surface elevation define a Dirichlet boundary value problem for each term of the expansion in the domain below the mean water level. The solution of these problems is sought in the form of a Fourier expansion by modal functions satisfying the Laplace equation and the boundary conditions at side boundaries and the bottom. This makes it possible to express the components of the vertical velocity at the free surface via modal coefficients, which themselves are defined by the surface elevation and the surface potential. This closes the evolution equations provided by the free surface conditions and allows to update the surface values. Fast Fourier Transforms are used to switch between spectral and physical spaces. The shape of the domain should be selected to define a simple spectral basis to expand the velocity potential. Therefore, either periodic domains in both horizontal dimensions or rectangular tanks are usually used.

An alternative approach uses the Dirichlet-Neumann (DN) operator, which expresses the normal surface velocity in terms of velocity potential at the surface. If such an operator is defined, the water wave problem is reduced to the integration over time of free-surface boundary conditions with unknown functions evaluated only at the free surface. The nonlinear DN operator is expanded in terms of a convergent Taylor expansion about the mean water level. This method was introduced by Craig and Sulem (1993) for 2D waves and extended by Bateman et al. (2001) to 3D cases. Schäffer (2008) demonstrated that different variants of HOS methods and methods that used DN operator are either identical or have only minor differences. The use of the additional potential allowed the modelling of a wavemaker (Ducrozet et al., 2012b) and a variable bathymetry (Gouin et al., 2016). This makes the HOS approach acceptable for numerical wave tanks. High efficiency and accuracy of spectral methods compare to other methods for wave propagation was demonstrated by Ölmez and Milgram (1995) and Ducrozet et al. (2012a).

One of the drawbacks of the spectral methods is that they can not model the overturning waves. However, this can not be considered as a serious disadvantage compared to the BEM and FEM models, if we consider their application to wave propagation. Neither of the models considered here is able to continue calculations after wave breaking. However, to model severe sea states and extreme waves, a model should continue calculations after waves break and provide a reasonable prediction of energy dissipation due to breaking. Seiffert and Ducrozet (2018) solved this problem by introducing

eddy viscosity as a diffusive term to the free surface boundary conditions to simulate breaking waves in a HOS model. Breaking onset is determined by a breaking criterion. The model demonstrated an impressive comparison with experiments on the propagation of surging wave groups.

More details on formulation and application of HOS models can be found in Bonnefoy et al. (2010).

2.4. Fully Lagrangian models

Another method to describe water waves is to use equations of fluid motion in the Lagrangian formulation. These equations are written in coordinates moving with the fluid. Each material point of the fluid continuum is labelled with a specific label, and the labels in the fluid-occupied domain create a continuous set of coordinates. These are Lagrangian coordinates or Lagrangian labels. Equations of fluid motion are solved in a fixed Lagrangian domain with the free surface represented by a fixed domain boundary. Some numerical methods use elements of the Lagrangian description. For example MEL free surface treatment by BEM and FEM described above. The SPH approach can be considered as fully Lagrangian. In this method, the fluid domain is represented by a set of material particles which serve as physical carriers of fluid properties. An integral operator with a compact smoothing kernel is used to represent the average properties of the fluid at a certain location, which are used to satisfy the equations of fluid motion. Each particle interacts with nearby particles from a domain specified by the smoothing kernel (e.g. Gomez-Gesteira et al., 2010; Violeau and Rogers, 2016). However, SPH does not directly refer to the equations of fluid motion in Lagrangian coordinates and should be distinguished from the methods where Lagrangian equations are directly applied to solve water wave problems.

The initial works on discrete approximation of equations of fluid motion in Lagrangian formulation with applications to water wave problems appeared in the early 70s. Brennen and Whitney (1970) used kinematic equations of mass and vorticity conservation for internal points of a domain occupied by an ideal fluid. Flow dynamics were determined by a free-surface dynamic condition. According to Fenton (1999) this approach apparently had not been followed and there are just a few works in which it was used (e.g. Nishimura and Takewaka, 1988). An alternative approach was developed by Hirt et al. (1970) who applied the equations of motion of viscous fluid in material coordinates moving together with fluid. The next step was the development of an Arbitrary Lagrangian-Eulerian (ALE) formulation (Chan, 1975). ALE

formulation uses a computational mesh moving arbitrarily within a computational domain to optimise the shape of computational elements and the problem is formulated in moving coordinates connected to the mesh. At certain regions of a computational domain the formulation can be reduced either to Eulerian (fixed mesh) or to fully Lagrangian (mesh moving with fluid) depending on the problem requirements. The Lagrangian models mentioned so far use quadrangular numerical cells. These models are subject to "alternating errors" and "even-odd" instability (Hirt et al., 1970; Chan, 1975), which is similar to the saw-tooth instability of the ALE approach. Moreover, application of fully-Lagrangian models to viscous problems has serious limitations. Boundary layers, wakes, vortices and other viscous effects lead to complicated deformations of fluid elements and large variations of physical coordinates over cells of a Lagrangian computational mesh. To address these problems the method was generalised for irregular triangular meshes (Fritts and Boris, 1979) and used for development of finite element models (e.g. Ramaswamy and Kawahara, 1987). This method however remains out of the mainstream and only occasionally appears in the literature (e.g. Kawahara and Anjyu, 1988; Radovitzky and Ortiz, 1998; Staroszczyk, 2009). Implementation of a finite element approach with irregular triangular meshes for ALE formulation (Braess and Wriggers, 2000) led to the development of a sophisticated method capable of solving complicated problems with interfaces including surface waves and fluid-structure interaction. A detailed description of the ALE method, examples of application and comprehensive bibliography can be found in Souli and Benson (2013). Finite element Lagrangian models and especially ALE models are complicated in both formulation and numerical realisation and are missing the main advantage expected from a Lagrangian method: simplicity of representing computational domains with moving boundaries. For many problems solved within the framework of ideal fluid deformation of the fluid domain remains comparatively simple. These problems can be efficiently approached by much simpler Lagrangian models similar to the original model of Brennen and Whitney (1970). Recent examples of application of such a model include tsunami waves in a wave flume (Buldakov, 2013), violent sloshing in a moving tank (Buldakov, 2014) and evolution of breaking wave groups (Buldakov et al., 2019).

A particular advantage of the Lagrangian models compared to the FNPT models is the ability to model vortical flows and therefore waves over sheared currents. Potential formulation assumes an irrotational flow and can therefore only be applied to a uniform current (Ryu et al., 2003; Chen et al., 2017).

Potential flow methods can also be generalised to flows with constant vorticity, which preserves the linearity of the problem. This allows the modelling of currents with linear profiles (e.g. Da Silva and Peregrine, 1988). On the other hand, in the inviscid Lagrangian formulation, vorticity does not change over time and can be generally defined as a function of Lagrangian labels. This allows a simple application to waves on arbitrary sheared currents. An example of such application can be found in Buldakov et al. (2015) and Chen et al. (2019). This feature of the Lagrangian formulation can also be useful for simulation of wave behaviour after breaking, which generates intensive vortical motion beneath the surface.

3. Lagrangian numerical wave model

Later in this chapter we consider a two-dimensional fully Lagrangian finite-difference wave model. The model follows the approach of the early Lagrangian models originally introduced by Brennen and Whitney (1970) and was further developed in Buldakov (2013, 2014) and Buldakov et al. (2019). Before continuing, let us first examine some aspects of the Lagrangian description that affect the application of discrete numerical methods, such as finite differences.

One of the main advantages of the Lagrangian approach is that the domain occupied by the fluid in Lagrangian coordinates remains the same during the fluid motion. The form of the Lagrangian domain is arbitrary. The only restriction is that mapping from Lagrangian to physical coordinates should not be singular. Therefore, the computational domain can be chosen by considering the convenience of numerical analysis. For example, a rectangular Lagrangian domain with sides parallel to the axes of the Lagrangian coordinate system can be selected. This greatly simplifies a numerical formulation since the finite difference approximation does not include cross terms. On the other hand, other aspects of the Lagrangian approach make its implementation more difficult, For example, there are situations where the boundary conditions of a part of the boundary change. This is the case for the self-contact of the different parts of the free surface during wave breaking, for the problems of entry and exit of solid bodies, the impacts of wave peaks with high structures, etc. However, for a large class of flows, a particle originally on a specific type of boundary (e.g. a free surface or a solid surface) remains on that boundary and the type of boundary condition does not change. This assumption provides a significant simplification in the

formulation of the problem and is used in the Lagrangian formulation considered in this work. In physical coordinates, the fluid domain can significantly change its original form. While strong local deformations, e.g. at the peaks of high waves, do not present a problem for a Lagrangian model, the continuous deformation of the entire volume of the fluid can present significant difficulties in the practical realisation of a Lagrangian formulation. This can be the case for domains with open boundaries. Examples are the Stokes' drift of a regular wave train or waves propagating over sheared currents. To overcome this problem one can apply relabelling, when a physical domain of a suitable shape is mapped into a new space of Lagrangian labels. A practical realisation of this approach is demonstrated later in this chapter, when we consider the application of the Lagrangian model to wave over sheared currents. For a compact travelling wave group the total deformation of the initial fluid volume is finite and such problems are ideal for application of Lagrangian wave formulation.

3.1. Mathematical formulation

Fluid motion in Lagrangian method is described by tracing marked fluid particles. For two-dimensional motion we have

$$x = x(a, c, t); \quad z = z(a, c, t),$$

where (x, z) are Cartesian coordinates of a particle marked by Lagrangian labels (a, c) at time t. Due to volume conservation for incompressible fluid the Jacobian J of a mapping $(x, z) \to (a, c)$ is a motion invariant: $\partial J/\partial t = 0$. This leads to the following Lagrangian form of the continuity equation:

$$J = \frac{\partial(x, z)}{\partial(a, c)} = J(a, c)\,, \tag{1}$$

where $J(a, c)$ is a given function of Lagrangian coordinates.

Equations of motion of inviscid incompressible fluid in Lagrangian coordinates (a, c) can be obtained using Hamilton's variational principle (e.g. Herivel, 1955). Let us represent the density of the Lagrangian in the following form

$$\mathcal{L} = \mathcal{T} - \mathcal{U} + \rho\, P(a, c, t)\,(J - J(a, c)),$$

where the kinematic continuity condition (1) is enforced by the Lagrange multiplier P, and ρ is fluid density. The densities of the kinetic and potential

energies of the fluid are

$$\mathcal{T} = \rho\,(x_t^2 + z_t^2)/2; \quad \mathcal{U} = \rho\, g\, z\,.$$

According to Hamilton's principle, the variation of the action integral

$$\delta I = \delta \int_{t_1}^{t_2} dt \iint_D \mathcal{L}\, da\, dc = 0$$

is zero, where the integration takes place in the Lagrangian space over a domain D occupied by the fluid. Taking the variation leads to the following equations describing dynamics of the fluid inside D

$$x_{tt} + \frac{\partial(P,z)}{\partial(a,c)} = 0\,; \quad z_{tt} + \frac{\partial(x,P)}{\partial(a,c)} + g = 0\,.$$

The Lagrange multiplier P can be recognised as the ratio of pressure over density and the boundary condition on the free surface $c = 0$ is $P = 0$. These equations can be resolved with respect to the spatial pressure derivatives and rewritten in the following form (Lamb, 1932)

$$\frac{\partial P}{\partial a} + g\, z_a = -x_{tt}x_a - z_{tt}z_a\,; \quad \frac{\partial P}{\partial c} + g\, z_c = -x_{tt}x_c - z_{tt}z_c. \tag{2}$$

The terms on the left hand sides of (2) are gradient components of a certain scalar function in the label space. Taking the curl of both sides of (2) we find that the value

$$\Omega = \nabla_a \times (x_t x_a + z_t z_a, x_t x_c + z_t z_c)$$

is a motion invariant: $\partial\Omega/\partial t = 0$, where $\nabla_a\times$ is the curl operator in (a,c)-space. This gives the second kinematic condition in addition to (1)

$$\Omega = \frac{\partial(x_t,x)}{\partial(a,c)} + \frac{\partial(z_t,z)}{\partial(a,c)} = \Omega(a,c), \tag{3}$$

where $\Omega(a,c)$ is a given function. This is the Lagrangian form of vorticity conservation and for irrotational flows $\Omega = 0$. Functions $J(a,c)$ and $\Omega(a,c)$ from (1) and (3) are defined by the initial conditions. $J(a,c)$ is defined by the initial positions of fluid particles associated with labels (a,c) and $\Omega(a,c)$ by the velocity field at $t = 0$.

The Lagrangian formulation does not require a kinematic free-surface condition, which is satisfied by specifying a fixed boundary of Lagrangian fluid domain corresponding to a free surface, e.g. $c = 0$. The dynamics of the flow is described by a dynamic free-surface condition which can be obtained from the first equation in (2). For a case of constant pressure on the free surface $c = 0$ we have

$$x_{tt}x_a + z_{tt}z_a + g\, z_a \,\big|_{c=0} = 0\,. \tag{4}$$

This condition has a simple physical meaning. The left-hand side of (4) can be written as a dot product of two vectors $\mathbf{a} = (x_{tt}, z_{tt} + g)$ and $\mathbf{t} = (x_a, z_a)$. The first vector is the acceleration of a fluid particle with subtracted gravity acceleration, and the second vector is tangential to the free surface. Therefore, the condition $\mathbf{a} \cdot \mathbf{t} = 0$ means that part of the acceleration of a fluid particle on the free surface produced by other fluid particles is normal to the free surface. The general formulation of the problem consists, therefore, of the continuity equation (1), the vorticity conservation equation (3), the free-surface condition (4) with suitable conditions on the bottom and side boundaries. Positions and velocities of fluid particles must be supplied as initial conditions.

One of the advantages of Lagrangian formulation is that the Lagrangian domain and the original correspondence between the physical and Lagrangian coordinates is arbitrary and can be chosen from convenience of numerical or analytical analysis. The only restriction is that the Jacobian J of the original mapping from Lagrangian to physical coordinates $(a, c) \to (x, z)|_{t=0}$ is not singular. It is convenient to use a rectangular Lagrangian domain

$$a_{\min} \le a \le a_{\max}; \quad -h \le c \le 0$$

where $c = -h$ corresponds to the bed, $c = 0$ to the free surface, $a_{\min}$ and $a_{\max}$ to the side boundaries (finite or infinite) of a physical domain and h is a characteristic depth, for example the mean still water depth.

A specific problem within the general formulation (1, 3, 4) is defined by the boundary and initial conditions specified for the Lagrangian domain. For a wave propagation problem, the boundary and initial conditions are used for wave generation. It is, for example, possible to specify the initial shape of a physical fluid domain and initial velocities corresponding to the kinematics of a periodic wave or other suitable boundary conditions on side boundaries. This, however, requires knowledge of wave kinematics, which in case of non-linear waves is not normally known and generating such kinematics is one

of the primary aims of solving the Lagrangian wave propagation problem. It is more convenient to solve a problem of wave evolution in a wave tank. Though this approach may have problems with reflections from boundaries of a finite domain similar to those of physical wave tanks, its numerical realisation is relatively simple and direct modelling of physical wave flumes makes it possible to have direct comparison between numerical and experimental results. The initial conditions in such approach can be still water conditions and waves can be generated by moving boundaries.

The boundary conditions for a wave tank problem can be formulated as follows. The known shape of the bottom provides the condition on the lower boundary $c = -h$ of the Lagrangian domain

$$F(\, x(a, -h, t), z(a, -h, t)\,) = 0\,, \tag{5}$$

where F is a given function. If we consider waves in a wave tank, conditions on the left and right boundaries of the Lagrangian domain $a = a_{\max}$ and $a = a_{\min}$ specify the shape of the basin walls

$$\begin{aligned} x(a_{\min}, c, t) &= X_L(\, z(a_{\min}, c, t),\, t\,) \\ x(a_{\max}, c, t) &= X_R(\, z(a_{\max}, c,\, t), t\,), \end{aligned} \tag{6}$$

where X_L and X_R are given functions of z and t. The dependence from x can be used to define the shape and the dependence from t the motion of a wavemaker.

3.2. Numerical scheme

For convenience of numerical realisation, we modify the original problem (1, 3 ,4) and write it in the following form

$$\Delta_t \left(\frac{\partial(x, z)}{\partial(a, c)} \right) = 0; \qquad \Delta_t \left(\frac{\partial(x_t, x)}{\partial(a, c)} + \frac{\partial(z_t, z)}{\partial(a, c)} \right) = 0 \tag{7}$$

where the operator Δ_t denotes the change between time steps. From the point of view of a numerical realisation, equations (7) mean that values in brackets at two time steps are equal to one another. This formulation does not require explicit specification of functions $J(a, c)$ and $\Omega(a, c)$, which are specified implicitly by initial conditions. We also modify the dynamic free

surface condition by adding various supplementary artificial and physical terms on the right-hand side

$$x_{tt}x_a + z_{tt}z_a + g\,z_a = -RHS(a,t)\Big|_{c=0}. \tag{8}$$

We use the following set of additional terms

$$RHS(a,t) = k\,(x_t\,x_a + z_t z_a) \;+\; \sigma\,\frac{\partial}{\partial\,a}\,\frac{\partial\,\kappa}{\partial\,t} \;+\; \gamma\,\frac{\partial\kappa}{\partial a} \;+\; P_a(a,t)\,. \tag{9}$$

where κ is the surface curvature. The first term in (9) introduces damping of displacement of surface particles with the damping coefficient $k(a)$. This term is used for absorbing waves approaching a boundary of a numerical wave tank opposite to a wavemaker and minimising reflections. The second term represents damping of surface curvature and $\sigma(a)$ is the corresponding damping coefficient. As described later in this chapter, it is used to simulate the dissipative effects of wave breaking. The third term represents surface tension. The coefficient γ is the ratio of the surface tension over density. In calculations presented in this work we use the value of $\gamma = 0.00073\,\mathrm{m}^3/\mathrm{s}^2$ corresponding to fresh water at 20°C. The last term is the prescribed surface pressure gradient, which can be used to create a pneumatic wave generator. The set of equations (7) with boundary conditions (8, 5, 6) is solved numerically using a finite-difference technique described below.

Since equations (7) for internal points of a computational domain include only first order spatial derivatives, a compact four-point Keller box scheme (Keller, 1971) can be used for finite-difference approximation of these equations. For our selection of the Lagrangian computational domain the stencil box can be chosen with sides parallel to the axes of the Lagrangian coordinate system, which significantly simplifies the final numerical scheme. The values of the unknown functions x and z on the sides of the stencil box are calculated as averages of values at adjacent points and then used to approximate the derivatives across the box by first-order differences. The scheme provides the second-order approximation for the box central point. Time derivatives in the second equation in (7) are approximated by second-order backward differences. It should be noted that the same scheme can be constructed by applying conservation of volume and circulation to elementary rectangular contours with linear approximation of unknown functions on boundaries of elementary volumes. Spatial derivatives in the free-surface boundary condition (8) are approximated by second-order central differences

and second-order backward differences are used to approximate time derivatives. As demonstrated below, this leads to a stable numerical scheme with weak dissipation. The overall numerical scheme is of second order accuracy in both time and space.

For finite-difference approximation of a boundary-value problem the number of algebraic mesh equations must be equal to the number of unknown values of functions at grid nodes. Let us consider a finite-difference approximation of the problem (7, 8, 5, 6) on a rectangular $N \times M$ mesh, where N and M are the numbers of mesh points in a and c directions. We are required to calculate values of unknown functions x and z at each mesh point. This gives $2 \times N \times M$ unknowns which should be determined by solving the same number of finite difference equations. Keller-box approximation of (7) gives two equations for every mesh cell or $2 \times (N-1) \times (M-1)$ equations. Approximation of boundary conditions (8, 5, 6) at internal points of corresponding boundaries results in $2 \times (N-2) + 2 \times (M-2)$ equations. Numerical tests demonstrated that both bottom condition (5) and vertical wall conditions (6) should be satisfied at lower corner points to provide their stability (4 equations). The last two equations are provided by vertical boundary conditions (6) at upper corner points. Altogether this adds up to the required $2 \times N \times M$ equations.

A fully-implicit time marching is applied, and Newton method is used on each time step to solve the nonlinear algebraic difference equations. It is important to note that the scheme uses only 4 mesh points in the corners of the box for internal points of the fluid domain. Therefore, the resulting Jacobi matrix used by nonlinear Newton iterations has a sparse 4-diagonal structure and can be effectively inverted using algorithms which are faster and less demanding for computational memory than general algorithms of matrix inversion. The current version of the solver uses a standard routine for inversion of general sparse matrices (NAG, 2016). To reduce calculation time, the inversion of a Jacobi matrix is performed at a first step of Newton iterations and if iterations start to diverge. Otherwise, a previously calculated inverse Jacobi matrix is used. Usually only one matrix inversion per time step is required. To start time marching, positions of fluid particles at three initial time steps should be provided, which specifies initial conditions for both particle positions and velocities. An adaptive mesh is used in the horizontal direction with an algorithm based on the shape of the free surface in Lagrangian coordinates $z(a, 0, t)$ to refine the mesh at each time step in regions of high surface gradients and curvatures. Constant mesh refinement

near the free surface is used in the vertical direction.

Since the finite-difference approximation presented above uses quadrangular mesh cells, it may be subjected to the so called alternating errors caused by non-physical deformations of cells (Hirt et al., 1970; Chan, 1975). This deformation preserves the overall volume (area) of a cell, as prescribed by finite difference approximation of the Lagrangian continuity equation. However, volumes of triangles build on cell vertexes can change. The area of one of the triangles increases while the area of the second triangle decreases by the same value. For a cell which is originally rectangular, this corresponds to trapezoidal deformation. This effect finally leads to alternating trapezoidal distortions of neighbouring cells occupying the whole domain, resulting in instability of short-wave disturbances with a wavelength equal to two cell spacing. In earlier models was usual to implement artificial smoothing to suppress this instability (e.g Chan, 1975). For the current model, efficient suppression of the instability caused by alternating errors is provided by an adaptive mesh. After several time steps the solution is transferred to a new mesh using quadratic interpolation. The effect of this procedure is similar to regridding used by Dommermuth and Yue (1987b). It reduces short-wave disturbances and does not produce unwanted damping. Alternating errors still remains the main reason for calculations breakdown. However, this happens for a large deformation of the computational domain associated with continuity breakdown of a physical domain caused, for example, by wave breaking. Otherwise, the numerical scheme proves to be stable with respect to this type of instability.

3.3. Numerical dispersion relation and dispersion correction

Special attention must be paid to approximation of second time derivatives in the free surface condition (4) since it defines the form of the numerical dispersion relation and is crucial for the overall stability of the scheme. For simplicity let us first consider a case of continuous spatial field in (1, 3, 4) combined with implicit discrete time approximation in (4). Let us approximate second derivatives by 3-point backward differences and expand this approximation to Taylor series with respect to a small time step τ. We get

$$\frac{f(t-2\,\tau)-2\,f(t-\tau)+f(t)}{\tau^2} = f''(t)-\tau\,f'''(t)+O(\tau^2)\,. \qquad (10)$$

As can be seen, the approximation is of the first order with the leading term of the error proportional to the third derivative of a function, which

gives the main contribution to the error of the dispersion relation. Under an assumption of small perturbations of original particle positions we represent unknown functions in the form

$$x = a + \varepsilon\,\xi(a,c,t); \quad z = c + \varepsilon\,\zeta(a,c,t)$$

and keep only linear terms of expansions with respect to the small displacement amplitude $\varepsilon \to 0$. Introducing a displacement potential ϕ

$$\xi = \partial\phi/\partial a; \quad \zeta = \partial\phi/\partial c$$

we satisfy the vorticity conservation (3) to the first order as $\varepsilon \to 0$ and the corresponding approximation of the continuity equation (1) is the Laplace equation for ϕ. The dynamic surface condition (4) becomes

$$\phi_a'' + g\,\phi_{ac} - \tau\,\phi_a{}''' = O(\tau^2)\,, \tag{11}$$

where primes denote time derivatives and only the leading term of the approximation error from (10) is taken into account. To derive the numerical dispersion relation we are looking for a solution in the form of a regular wave in deep water:

$$\phi = e^{i\,k\,a}\,e^{k\,c}\,e^{i\,\omega\,t}\,,$$

which satisfies the Laplace equation. The dynamic condition (11) is satisfied when ω and k are related by a dispersion relation. Similar analysis can be performed for higher orders of approximation of the derivatives. Below is the summary of dispersion relations obtained for orders $n = 1 \ldots 4$:

$$\omega/\sqrt{gk} = \pm 1 + \frac{1}{2}\,i\,\hat\tau + O(\hat\tau^2)\,; \tag{12a}$$

$$\omega/\sqrt{gk} = \pm 1 \mp \frac{11}{24}\,\hat\tau^2 + \frac{1}{2}\,i\,\hat\tau^3 + O(\hat\tau^4)\,; \tag{12b}$$

$$\omega/\sqrt{gk} = \pm 1 - \frac{5}{12}\,i\,\hat\tau^3 + O(\hat\tau^4)\,; \tag{12c}$$

$$\omega/\sqrt{gk} = \pm 1 \pm \frac{137}{360}\,\hat\tau^4 - \frac{19}{24}\,i\,\hat\tau^5 + O(\hat\tau^6)\,. \tag{12d}$$

We use a nondimensional expansion parameter $\hat\tau = \sqrt{gk}\,\tau$, which is the measure of the problem discretisation representing the ratio of the time step to a typical problem period. As can be seen, the first-order scheme (12a)

introduces numerical viscosity proportional to $\hat{\tau}$ which leads to fast non-physical decay of perturbations. The higher-order schemes (12c,12d) include terms proportional to $-i$, leading to growth of perturbations, making the numerical scheme unstable. We therefore use the second-order scheme (12b), which incorporates a numerical error to dispersion at the second order $\hat{\tau}^2$ and a weak third order ($\hat{\tau}^3$) dissipation term.

Let us now include spatial discretisation according to the numerical scheme described above with discretisation steps $(\delta a; \delta c)$. As before, we consider a linearised approximation for a regular travelling wave in deep water. However, differential approximation of the discretised field equations (1,3) includes higher spatial derivatives and the solution can not be represented in the form of the displacement potential. A suitable form of the solution is

$$\xi = i\, e^{i\,k\,a}\, e^{\varkappa\, c}\, e^{i\,\omega\, t}; \quad \zeta = e^{i\,k\,a}\, e^{\varkappa\, c}\, e^{i\,\omega\, t},$$

where the constant for the exponential decay of displacement with depth $\varkappa$ is not equal to the wavenumber. The expression for $\varkappa$ to satisfy the discrete versions of (1) and (3) can be found as an expansion by discretisation parameters. As before, the expansion for ω defines the numerical dispersion relation and is used to satisfy the free-surface condition (4). The corresponding expansions are found to be

$$\varkappa/k = 1 - \frac{1}{24}\,(\,\delta\hat{a}^2 + \delta\hat{c}^2\,) + O(\delta\hat{a}^4; \delta\hat{c}^4) \tag{13}$$

and

$$\omega/\sqrt{gk} = \pm 1 \mp \frac{1}{24}\,(11\,\hat{\tau}^2 + 2\,\delta\hat{a}^2) + \frac{1}{2}\,i\,\hat{\tau}^3 + O(\hat{\tau}^4; \delta\hat{a}^4)\,,$$

where the nondimensional discretisation steps $\hat{\tau} = \sqrt{gk}\,\tau$, $\delta\hat{a} = k\,\delta a$ and $\delta\hat{c} = k\,\delta c$ are used. It is interesting to note that the dispersive error is affected only by horizontal discretisation step, while the vertical discretisation affects wave kinematics. Therefore, if we are interested in the evolution of the waveform alone, we can use relatively few vertical mesh points.

Validation tests presented later in this section show that the dispersion error is crucial for travelling wave and the achieved convergence rate for the second-order dispersion approximation is not sufficient. To increase the approximation order for the dispersion relation we introduce dispersion correction terms to the free surface boundary condition. These terms should satisfy the following conditions: (i) to have the order of $O(\tau^2; \delta a^2)$; (ii) to be

linear; (iii) not to include high derivatives; (iv) to use the same stencil as the original scheme and (v) to reduce the order of the dispersion error. It has been found that the free surface boundary condition (4) with the dispersion correction term satisfying these conditions can be written as follows

$$x_{tt}x_a + z_{tt}z_a + g\,z_a + \left(\frac{1}{6}\delta a^2\,x_{aa,tt} - \frac{11}{12}g\,\tau^2 z_{a,tt}\right) = 0\,\Big|_{c=0}\,, \qquad (14)$$

where the dispersion correction term is given in parentheses. The term x_{aa} with the second-order spatial derivative leads to high-wavenumber nonlinear instability for large wave amplitudes. To suppress this instability, we apply 5-point quadratic smoothing to the function $x(a)$ before applying the finite-difference operator. The smoothing is applied only to this term in (14). It is applied at the future time layer to ensure that the scheme remains fully implicit. It can be shown that the numerical dispersion relation becomes

$$\omega/\sqrt{gk} = \pm 1 + \frac{1}{2}\,i\,\hat{\tau}^3 \pm \left(\frac{361}{480}\hat{\tau}^4 - \frac{1}{360}\delta\hat{a}^4\right) - \frac{13}{12}\,i\,\hat{\tau}^5 + O(\hat{\tau}^6; \delta\hat{a}^6)\,. \qquad (15)$$

We now have weak numerical dissipation at 3-rd order and the dispersion error at 4-th order. A term with weak negative dissipation at 5-th order should also be noted. This term can potentially lead to solution instability for large time steps.

3.4. Numerical treatment of breaking

A disadvantage of numerical models of wave propagation considered in this chapter is their inability to model spilling breakers. The discontinuity of the free surface that develops at the spilling crest leads to a singularity in a numerical solution leading to a breakdown of the calculations. Models based on Lagrangian representation of the free surface (MEL and fully Lagrangian) can simulate overturning waves and, therefore, with sufficient spatial and temporal resolution they can resolve micro-plungers originating at wave crests during initial stages of spilling breaking. However, they are unable to continue the calculations after self-contact of the free surface occurs and the resulting solution becomes non-physical. This makes impossible applying such models to steep travelling waves and severe sea states.

Removing a singularity in the vicinity of the breaking crest can help in continuing calculations with only a minor effect on the overall wave behaviour. This can be achieved by implementing artificial local dissipation

in the vicinity of a wave crest prior to breaking. With this approach all small-scale local features would disappear from the solution, but the overall behaviour of the wave would still be represented with good accuracy. Practical implementation of the method includes using of a breaking criterion to initiate dissipation right before breaking occurs. The dissipation is usually enforced by including damping terms in the free-surface boundary conditions (Haussling and Coleman, 1979; Subramani et al., 1998; Guignard and Grilli, 2001). Recently, a breaking model based on an advanced breaking criterion and an eddy viscosity dissipation model was developed by Tian et al. (2012) and implemented in a spectral model of wave evolution (Tian et al., 2012; Seiffert and Ducrozet, 2018). The method demonstrates a good comparison with the experiments and allows to apply spectral models to simulate evolution of severe sea states with breaking.

In this chapter we use a method of treatment of spilling breaking which uses the same basic concept but differs in the details of realisation. The method includes dissipative suppression of the breaker and correction of crest shape to provide accurate post-breaking behaviour of the wave. There are several conditions such a method should satisfy: (i) to act locally in the close vicinity of a developing singularity without affecting the rest of the flow; (ii) to simulate energy dissipation caused by breaking; (iii) to be mesh-independent, that is the change of the effect with changing mesh resolution should be within the accuracy of the overall numerical approximation and (iv) to be naturally included into a problem formulation representing an actual or artificial physical phenomenon. The development of a spilling breaker is associated with a rapid growth of surface curvature. Therefore, the local dissipation effect satisfying these conditions can be created by adding a term $-\sigma\,\partial/\partial a\,(\,\partial\kappa/\partial t\,)$ to the right hand side of the free surface dynamic condition (8,9). This term with a small coefficient σ introduces artificial dissipation due to the change of surface curvature κ which acts locally at around the region of fast curvature changes and suppresses breaker development without affecting the rest of the wave. To minimise the undesirable effect of dissipation, the action of the damping term is limited both in time and in space. Breaking dissipation is triggered when the maximal acceleration of fluid particles at the crest exceeds a specified threshold $a_{\rm on}$ and is turned off when the maximum acceleration falls below a second lower value $a_{\rm off}$. Spatially, the action of the breaking model is limited by the half-wavelength between the ascending and descending zero-crossing points delimiting a breaking wave crest.

Activation of the damping term makes it possible to continue the calculation beyond the breaking event. However, the resulting shape of the wave crest is different from the actual crest after the breaking. Since local dissipation suppresses breaking, the local behaviour of the wave crest is different from the real one. Overturning of the crest does not occur, and for a sufficiently intense breaking, it can significantly affect the shape of the entire wave around the crest. To account for this difference, we apply additional surface tension around the crest. Numerical tests show that large surface tension produces an effect similar to that of the peak overturning. It changes the shape of the crest and reduces the error in the profile of the post-breaking wave. This effect is achieved by the surface tension term in the right side of the free surface boundary condition (8,9) with an appropriately selected coefficient $\gamma_{\rm br}$ added to the natural value of γ. It should be emphasised that the desired effect is only possible for values of the $\gamma_{\rm br}$ much larger than the actual ones and it is used only in the regions and during the periods when the breaking model operates.

To summarise, the intensity of the dissipation (σ), the acceleration thresholds to activate and deactivate the dissipation ($a_{\rm on}$ and $a_{\rm off}$) and the strength of the surface tension for the correction of the shape of the crest ($\gamma_{\rm br}$) constitute the four parameters of the breaking model. The functions of the parameters of the model are as follows. Parameter $a_{\rm on}$ defines the beginning of the breaking process, σ regulates the rate of energy dissipation, $a_{\rm off}$ controls the duration of the breaking and the total amount of energy dissipated and $\gamma_{\rm br}$ corrects the shape of the breaking crest. It should be noted that being a heuristic model, the breaking model requires calibration of parameters to achieve optimal performance for each particular case. For this paper, the parameters were selected by running a small number of numerical cases for different parameters values. The following values of the parameters are selected for calculations presented below: $a_{\rm on} = g$, $a_{\rm off} = g/2$, $\sigma = 0.0002\,{\rm m}^3/{\rm s}$ and $\gamma_{\rm br} = 0.01\,{\rm m}^3/{\rm s}^2$. Additional work is required for systematic study of the effects of the parameters on model performance and to establish a rational procedure of selecting parameters for different breaking conditions.

3.5. Numerical efficiency

An important question is the computational efficiency of the model. In the implicit time marching scheme implemented in the Lagrangian solver, the most time consuming element is the inversion of a Jacobi matrix used by

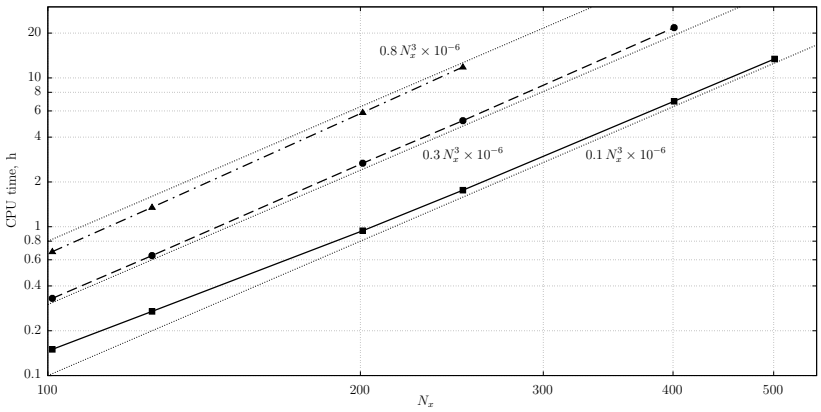

Figure 1: Computation time for modelling of 20 sec of wave propagation by the Lagrangian solver on a single 2.4 GHz CPU for different mesh size: $N_z = 11$ (solid); $N_z = 16$ (dashed); $N_z = 21$ (dash-dotted).

the Newton iterations for solving nonlinear grid equations. The required calculation time grows fast with increasing the matrix dimension, which equals to the number of mesh equations and is proportional to the product of the dimensions of a numerical mesh. For a matrix inversion algorithm used in this work, the inversion time is approximately proportional to the square of the dimension of the matrix. For a 2D problem with a constant value of N_z much smaller than N_x, the matrix dimension is proportional to N_x. To provide a uniform discretisation error in space and time, the value of time step should be proportional to δx which implies that the number of steps is proportional to N_x. Thus, the overall calculation time grows with a rate proportional to N_x^3, as illustrated by Figure 1 for the numerical presented in Table 1.

High demand for computational resources for large scale problems is a well recognised disadvantage of implicit schemes, which often outweighs their advantages in numerical stability. The radical method of increasing computational efficiency is using parallel computing. Implicit solvers have a single standard time-consuming operation and are therefore suitable for efficient parallelisation. A parallel version of an implicit solver can be created with minimal changes to the original code by replacing a matrix inversion subroutine with a parallel analogue. This feature is particularly useful in light of recent advances in GPU-based matrix inversion algorithms, which are much faster than conventional parallelisation using multiple CPUs (e.g. Sharma

N_x	N_z			δt, *sec*	N_x	N_z			δt, *sec*
101	11	16	21	0.010	251	11	16	21	0.004
126	11	16	21	0.008	401	11	16		0.0025
201	11	16	21	0.005	501	11			0.002

Table 1: Numerical cases for convergence and validation tests of the Lagrangian model.

et al., 2013).

3.6. Model validation

We validate numerical results against a set of experimental data on propagation of focussed wave groups obtained in a wave flume of the Civil Engineering department at UCL. The flume has the width of 45 cm and the length of the working section between two piston wavemakers is 12.5 m (see Figure 2). A paddle on the right end of the flume is used as a wave generator and the opposite paddle as an absorber. Water depth over the horizontal bed of the flume was set to $h = 40$ cm. We use the centre of the flume as the origin of the coordinate system with the x-axis directed towards the wave generator positioned at $x = 6.25$ m. The vertical z-axis with the origin at the mean water surface is directed upwards. The wavemaker uses a control system with force feedback operating in a frequency domain, which allows precise control and partial absorption of incident waves to reduce reflections. The input of the control system is the desired linear amplitude spectrum of the target wave at the centre of the flume. The control system uses discrete spectrum and generates periodic paddle motions. For our experiments we used an overall return period of 128 sec, which is the time between repeating identical events produced by the paddle. This means that the wavemaker generates the discrete spectrum with frequencies $n/128$ Hz, where n is the integer. We use $n = 1 \ldots 512$ to generate 512 frequency components in the range from 1/128 to 4 Hz. Generated waves were monitored by a series of resistance wave probes measuring surface elevation, and an ultrasonic sensor was used to record paddle motion.

We apply an iterative procedure (Buldakov et al., 2017) to generate a Gaussian wave group with peak frequency of $f_p = 1$ Hz focussed at the centre of the flume with the linear focus amplitude of 2.5 cm. Then, we use the resulting input spectrum to generate higher amplitude waves by multiplying

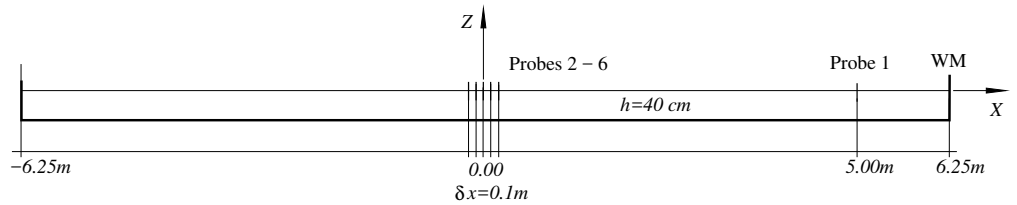

Figure 2: Wave flume layout and positions of wave probes.

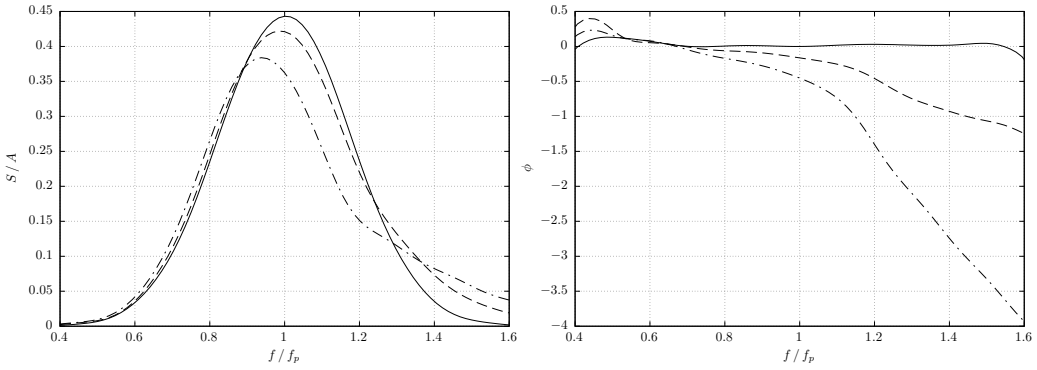

Figure 3: Linearised spectra of experimental wave groups at the focus point ($x = 0$). Amplitude (left) and phase (right). Solid– $A = 2.5\,\mathrm{cm}$; dashed– $A = 5\,\mathrm{cm}$; dash-dotted– $A = 7.5\,\mathrm{cm}$.

the input by factors 2 and 3 without further focussing or spectrum corrections. We therefore obtain waves with linear focus amplitudes $A = 5\,\mathrm{cm}$ and $A = 7.5\,\mathrm{cm}$. The linearised spectra of generated waves at $x = 0$ are shown in Figure 3. As can be expected, non-linear defocussing and transformation of the spectrum can be observed for higher amplitude waves. The linearisation is done using the spectral decomposition method described in (Buldakov et al., 2017), which requires generation of waves with 4 constant phase shifts $\Delta\phi = 0,\ \pi/2,\ \pi,\ 3\pi/2$. In this section we are using results with $\Delta\phi = 0$, which corresponds to a peak-focussed linear wave. The resulting waves are of tree distinct qualitative types. The small amplitude wave ($A = 2.5\,\mathrm{cm}$) has weakly non-linear features. The wave with $A = 5\,\mathrm{cm}$ can be described as a strongly nonlinear non-breaking wave. And the high amplitude wave ($A = 7.5\,\mathrm{cm}$) exhibits two intensive breaking events, while it travels along the flume.

We reconstruct the experimental setup using a numerical wave tank based on the previously described Lagrangian numerical model. The dimensions of

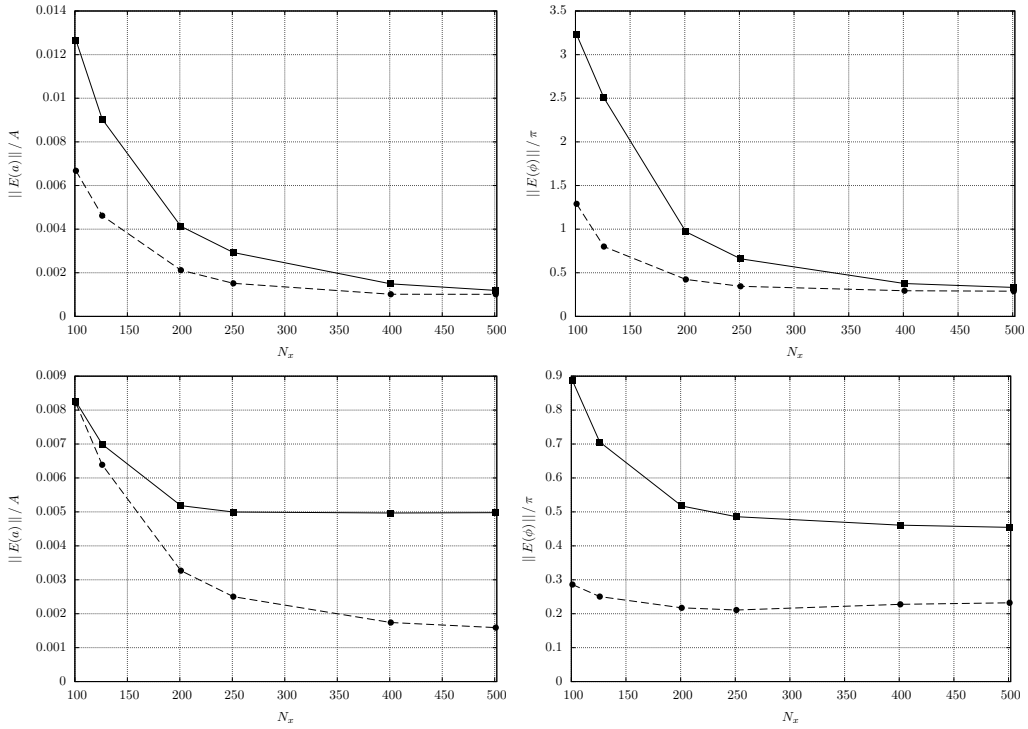

Figure 4: L_2-norm of difference between amplitude (left) and phase (right) spectra of a wave group at $x = 0$ measured in experiment and calculated by the Lagrangian solver. Top – $A = 5\,\mathrm{cm}$; without (solid) and with (dashed) dispersion correction. Bottom – $A = 7.5\,\mathrm{cm}$; breaking control without (solid) and with (dashed) crest correction. $N_z = 11$.

the NWT are the same as the dimensions of the experimental tank. The wave is generated by implementing the boundary condition (6) on the right boundary of the computational domain with $X_R(z,t)$ specified by the paddle displacement recorded in the experiment. To account for gaps between the paddle and walls and bottom of the experimental wave tank and for frictional losses at the wavemaker the amplitude of the numerical wave generator is reduced by 18.5%. The surface displacement damping term in (9) is activated near the tank wall opposite the wavemaker to absorb the reflections. Calculations are performed for all experimental cases, including 3 amplitude values and 4 phase shifts, and repeated with different time steps and horizontal and vertical numbers of mesh points. The time step has been reduced with an increasing number of horizontal mesh points to maintain the dispersion errors due to temporal and spatial discretisation as given by (15), approximately

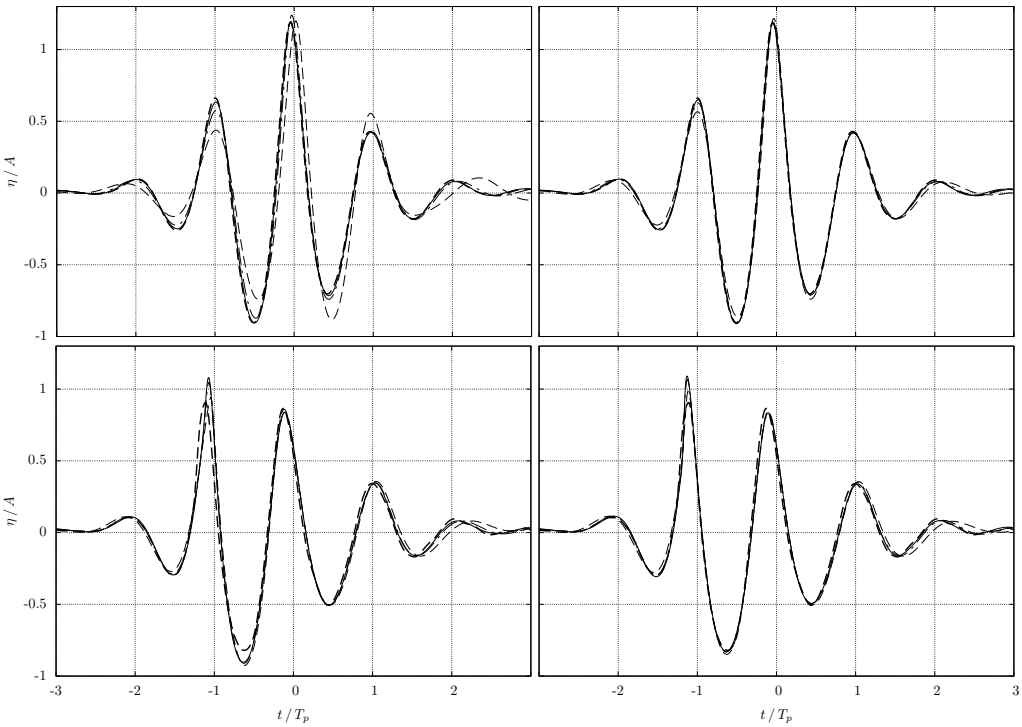

Figure 5: Convergence of time history of surface elevation for a wave group at $x = 0$. Experiment (thick dashed) and Lagrangian solver: $N_x = 101$ (dashed); $N_x = 201$ (dash-dotted); $N_x = 401$ (solid); $N_z = 11$. Top – $A = 5cm$ without (left) and with (right) dispersion correction. Bottom – $A = 7.5cm$, breaking control without (left) and with (right) crest correction.

equal to each other. This provides uniform convergence by both parameters. The summary of parameters for the numerical cases is given in Table 1.

The convergence is tested using an L_2 norm of the difference between the experimental and calculated spectral components of the surface elevation at the linear focus point $x = 0$. The norms for spectral amplitudes and phases are calculated as

$$||E(a)|| = \sqrt{\sum_i (a_i - a_{i_{\rm EXP}})^2}\,; \quad ||E(\phi)|| = \sqrt{\sum_i (\phi_i - \phi_{i_{\rm EXP}})^2}\,,$$

where the sum is taken over discrete spectral components in the range $0.5\,\mathrm{Hz} < f < 1.5\,\mathrm{Hz}$ from the set generated by the wavemaker ($n = 64 \ldots 192$), where the amplitude components are large enough not to be affected by experimen-

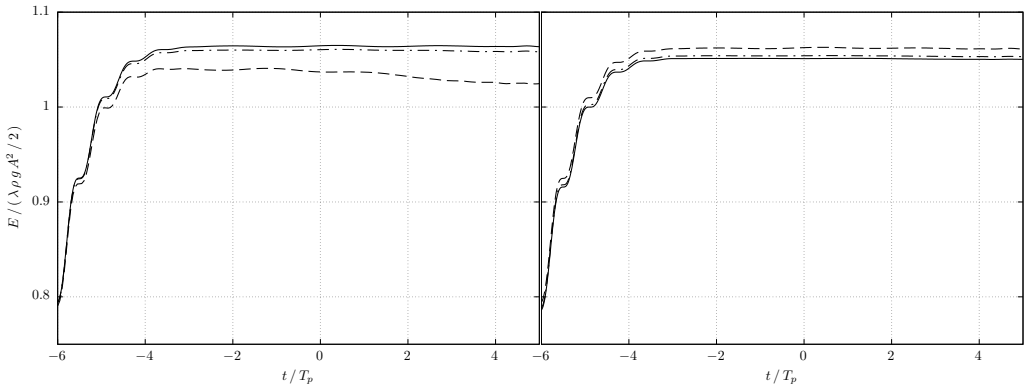

Figure 6: Convergence of the normalised total energy for the Lagrangian solver with dispersion correction. $A = 5\,\mathrm{cm}$. Left – increasing horizontal mesh resolution: $N_x = 101$ (dashed); $N_x = 201$ (dash-dotted); $N_x = 401$ (solid); $N_z = 11$. Right – increasing vertical mesh resolution: $N_z = 11$ (dashed); $N_z = 16$ (dash-dotted); $N_z = 21$ (solid); $N_x = 251$.

tal errors. It should be noted that full convergence of the calculated results to the experimental measurements can not be expected. The numerical model is based on a set of assumptions that are satisfied with limited precision. In addition, the measurements include some experimental errors. Therefore, the difference between the experimental and numerical results converges to a certain small value and does not change with an additional increase in the resolution of the numerical model.

The selected results of the convergence tests are presented in Figures 4-6. As can be seen in the top row of Figure 4, the results with and without dispersion correction converge to the same solution. However, the introduction of a dispersion correction considerably increases the speed of convergence for both amplitudes and phases. The experimental results can be reproduced with sufficient accuracy for a relatively small number of horizontal mesh points and a relatively large time step. For a breaking wave (Figure 4, bottom row), the shape correction of the crest introduces a new physical process. For this reason, the numerical results with and without crest correction converge to different solutions, and the numerical result with the correction shows a much better comparison with the experiment. A general impression of convergence and accuracy of the different versions of the numerical model can be obtained from the graphs of the time history of surface elevation presented in Figure 5.

Figure 6 shows the behaviour of the total wave energy in the wave tank

calculated for different temporal and horizontal resolutions and different resolutions of the vertical mesh. Wave absorption is disabled for energy tests. The energy is normalised by the energy of one wave length λ of a linear regular wave with the frequency and the amplitude equal to the peak spectral frequency the linear focus amplitude of the wave group. The kinetic energy is calculated by numerical integration over the entire Lagrangian fluid domain using a bi-linear interpolation of the velocities of the fluid particles inside mesh cells. This provides the second order approximation of the integral with respect to the mesh resolution. According to (13), the error of the velocity profiles within the fluid domain, and thus the kinetic energy, is determined by the horizontal and vertical resolution of the mesh. The potential energy is calculated as an integral of the potential energy density at the free surface and is not directly affected by the discretisation of the vertical mesh. As can be seen in Figure 6, the total energy in the tank increases up to $t \approx 4\,\text{sec}$ seconds due to the energy generated by the wave paddle. For low horizontal mesh resolution, the dissipative term in the numerical dispersion relation leads to the reduction of the energy of the propagating wave. For higher resolutions, energy conservation is satisfied with high accuracy. The right graph of Figure 6 shows the rapid convergence of energy with increased vertical resolution. This includes both the convergence of the numerical integral used to calculate kinetic energy and the convergence of the numerical solution for wave kinematics, as indicated by expansion (13). Overall, the convergence tests show that the numerical results converge towards a solution, which approximates the experiment with a good accuracy. The implementation of the dispersion correction term greatly increases the convergence rate and provides accurate results with a smaller number of mesh points and a larger time step.

4. Model application to the evolution of extreme wave groups

After validation of the model in the previous section, this section considers the performance of the model on the simulation of extreme wave groups with a focus on modelling the wave breaking process. All results presented in this section are calculated using a 401×16 mesh and the time step $\delta t = 0.0025\,\text{sec}$. Figure 7 shows the evolution of the total wave energy for different wave amplitudes and phase shifts $\Delta\phi = 0$ and $\Delta\phi = \pi$, which correspond to opposite wavemaker input signals. The wave energy increases from the initial zero level starting at $t \approx -14\,\text{sec}$, when the wavemaker begins to operate.

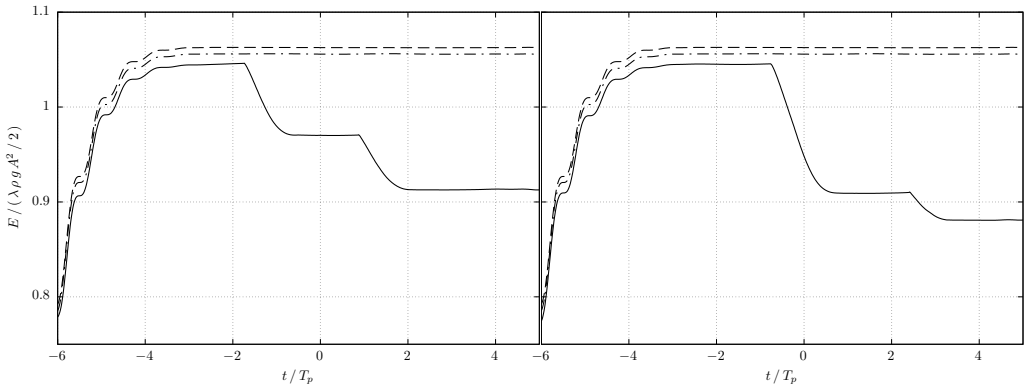

Figure 7: Normalised total wave energy for different wave amplitudes: $A = 2.5\,\mathrm{cm}$ (dashed); $A = 5\,\mathrm{cm}$ (dash-dotted) and $A = 7.5\,\mathrm{cm}$ (solid). Left – phase shift $\Delta\phi = 0$. Right – phase shift $\Delta\phi = \pi$.

After the wavemaker stops at $t \approx -3\,\mathrm{sec}$, the total energy remains constant until wave breaking occurs for high amplitude waves. As expected, the energy of non-breaking waves is the same for both phase shifts. It can be seen that for $\Delta\phi = 0$ there are two breaking events of similar intensity which are symmetrical with respect to $t = 0$ and with respect to the centre of the tank $x = 0$. For $\Delta\phi = \pi$, an intensive breaking event occurs near the centre of the tank close to $t = 0$ and a much smaller event later. This is confirmed by wave observations during the experiments. Later in this section, we will limit our attention to the large breaking event at the tank centre and consider the wave with $A = 7.5\,\mathrm{cm}$ and $\Delta\phi = \pi$.

Figure 8 shows the time history of wave crest elevation at three locations along the tank. The corresponding wave profiles can be seen in Figure 9. The difference between measured and calculated wave crests can be observed in Figure 8 near the top of the crest. It should be noted that for high wave peaks experimental measurements by wave probes are unreliable. High speed flow at the crest creates a cavity around the wave probe wires, which generates an error that reduces the recorded crest elevation. However, for the main part of the crest, the calculated and experimental results are compared with good accuracy. The rounded end of the overturning wave observed in Figure 9 is explained by the surface tension which produces a considerable effect on the relatively small experimental scale. At $x = 0.2\,\mathrm{m}$ the breaking model is not yet operational and the Lagrangian solutions with and without the breaking model are identical. At $x = 0$, the top of the wave crest begins

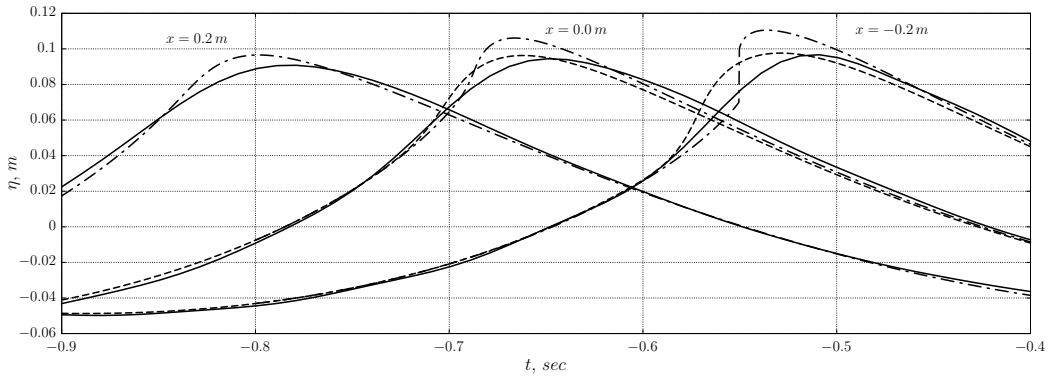

Figure 8: Time histories of wave crest evolution at different positions along the flume, $A = 7.5\,\text{cm}$, $\Delta\phi = \pi$. Experiment (solid); Lagrangian model (dash-dotted); Lagrangian model with breaking model (dashed).

to deform. It moves faster than the main body of the crest and eventually overturns. At this stage, the breaking model turns on the damping, and the shape of the crest with and without the breaking model becomes different. Farther along the tank, at $x = -0.2\,\text{m}$, the top of the crest begins to overturn and forms a vertical front. The shape of the crest with the operating breaking model differs considerably from the shape of the crest that evolves freely. However, the difference is located near the top of the crest and the rest of the wave is unaffected by the breaking model. Examples of horizontal and vertical velocity profiles at the wave crest and on the front and rear slopes are given in Figure 10. The profiles are presented at the moment when surface elevation reaches its maximum at $x = 0$ and when the overturning crest begins to develop. The difference between calculated velocities with and without breaking model can be observed near the top of the wave crest but quickly disappears everywhere else. Calculations without the breaking model are continued until the self contact of the overturning wave occurs at $t = -0.36\,\text{sec}$ (Figure 9). After that, the results produced by the Lagrangian model without the breaking model cease to be physically meaningful. The breaking model allows continuing calculations beyond this point. As can be seen in Figure 9, the solution with the breaking model reproduces relatively well the shape of the self-contacting wave crest, which provides a good starting point for further simulation of the post-breaking wave.

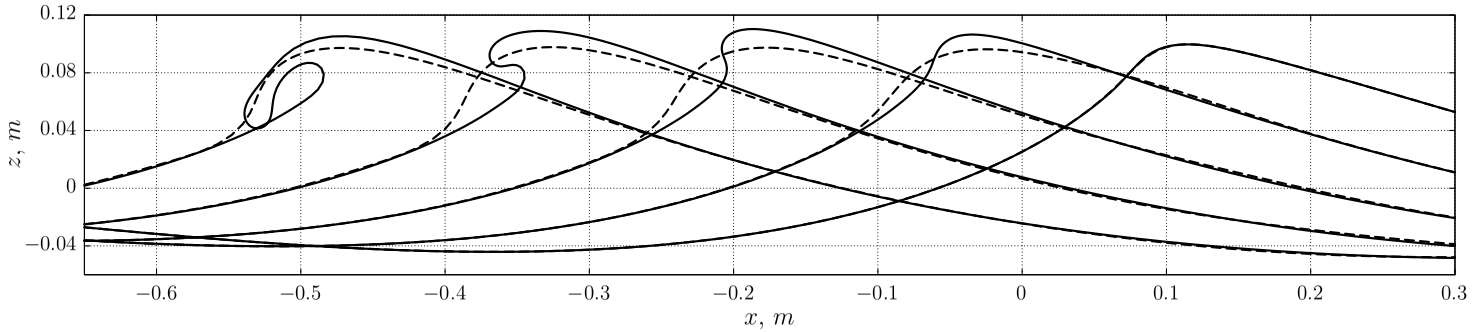

Figure 9: Breaking crest evolution between $t = -0.76\,\text{sec}$ and $t = -0.36\,\text{sec}$. Lagrangian model (solid); Lagrangian model with breaking model (dashed).

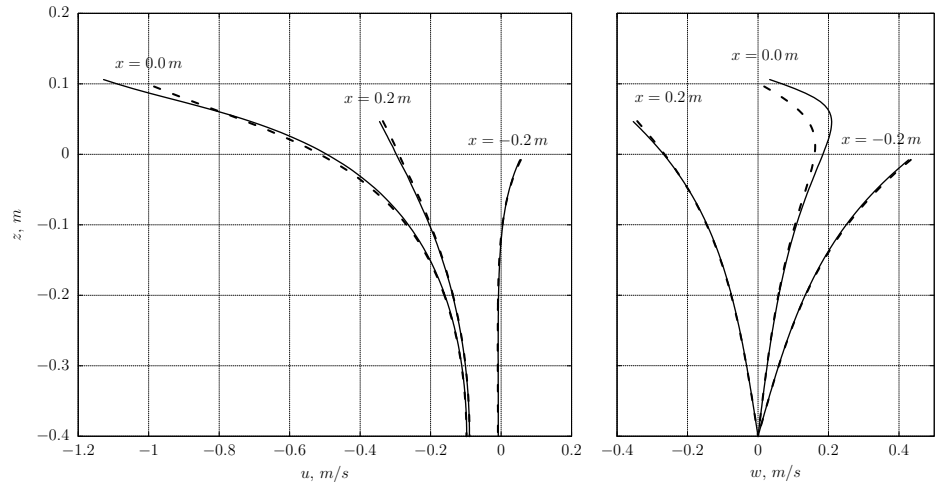

Figure 10: Horizontal (left) and vertical (right) velocity component profiles at $t = -0.665\,\mathrm{sec}$ and different positions along the flume. Lagrangian model (solid); Lagrangian model with breaking model (dashed). The time corresponds to the maximal surface elevation at $x = 0$.

5. Model application to waves on sheared currents

One of the advantages of the Lagrangian formulation is that it offers a simple treatment of flows with vorticity and is therefore suitable for modelling waves on sheared currents. A sheared current can be defined by specifying the vorticity that depends solely on the vertical Lagrangian coordinate c. For our choice of the Lagrangian labels the parallel current can be specified as $x = a + V(c)\,t;\ z = c$, where $V(c) = V(z_0)$ is the current profile. Substitution to (3) gives

$$\Omega(a, c) = \Omega(c) = V'(c)\,. \tag{16}$$

Therefore, the waves on a sheared current with an undisturbed profile $V(z_0)$ are described by equations (1, 3) with the free surface boundary condition (4), the bottom condition (5) and the vorticity distribution given by (16). As before, the numerical implementation is based on a form of the governing equations given by (7) and the free surface boundary condition with the dispersive correction (14) with additional terms in the right-hand side. For wave-current calculations we use the following additional terms

$$RHS = k(a)\,(\,(\,x_t - V(c)\,)\,x_a + z_t z_a) + P_x(x, t)\,x_a\,. \tag{17}$$

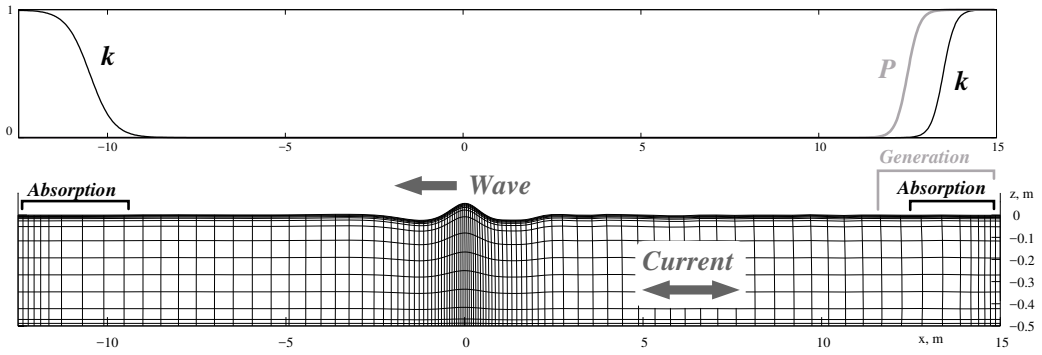

Figure 11: Schematic representation of the Lagrangian numerical wave-current flume. The upper graph demonstrates the shapes of distributions for the surface pressure P and the dissipation coefficient k from equation (17). Wave and current directions and wave generation and absorption zones are indicated.

The first term of (17) is the modified dissipation term and the second term is the time varying surface pressure gradient that is used for wave generation. The breaking model is not implemented in the wave-current version of the solver.

The numerical wave-current flume is created by specifying inlet and outlet boundary conditions, distribution of the surface dissipation $k(a)$ and the surface pressure gradient $P_x(x,t)$. The NWT design should provide free current inflow and outflow to and from the computational domain, wave generation on the current, and absorption of waves incident to the domain boundaries to eliminate reflections. The dissipation coefficient is set to zero in the working section of the flume. It gradually increases to a large value near the input and output boundaries to ensure a stable horizontal free surface that remains at the initial position $z = 0$. This provides parallel input and output flows and serves a double purpose. Firstly, the reflections from the boundaries are significantly reduced. Secondly, the inlet and outlet boundary conditions can be specified as the undisturbed velocity profile at the inlet and as a parallel flow at the outlet

$$x_t(a_{in}, c, t) = V(c); \quad z_a(a_{out}, c, t) = 0\,.$$

The wave is generated by creating an area in front of one of the wave absorption zones where the pressure distribution of a prescribed shape is defined. The time varying amplitude of the pressure disturbance is used as the control input for this pneumatic wave generator. It should be noted that the

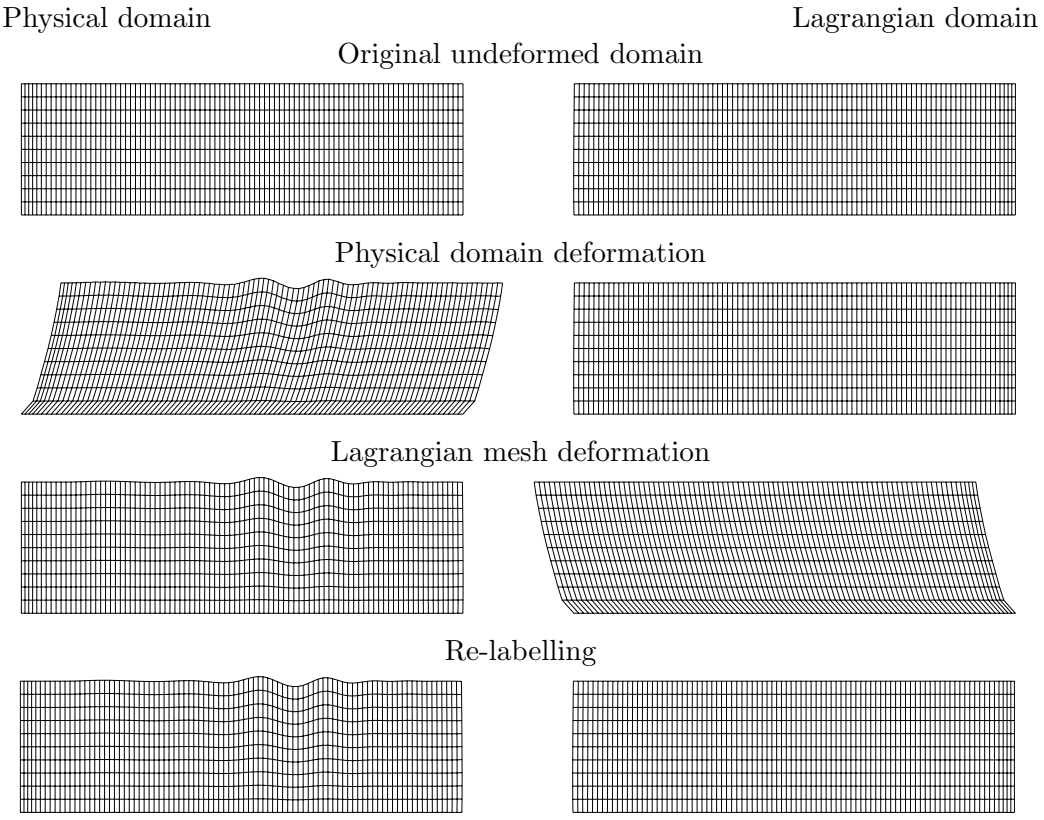

Figure 12: Diagram of the procedure of deformation and re-labelling of the Lagrangian mesh.

generated waves propagate in both directions, but the waves propagating backwards are damped by the first absorption zone. Figure 11 illustrates the setup of the Lagrangian numerical wave-current flume.

An additional difficulty with the numerical realisation of the Lagrangian formulation on sheared currents is the continuous deformation of the original physical domain. The accuracy of the calculations for highly deformed meshes decreases considerably. If the deformation is too strong, this can lead to calculations breakdown. To avoid these difficulties, we carry out shear deformation of the Lagrangian domain to compensate for the deformation of the physical domain. The deformation takes place after several time steps and brings the boundaries of the physical domain back to the vertical lines. After that, we re-label the fluid particles with new values of Lagrangian coordinates in order to preserve the rectangular shape of the Lagrangian computational

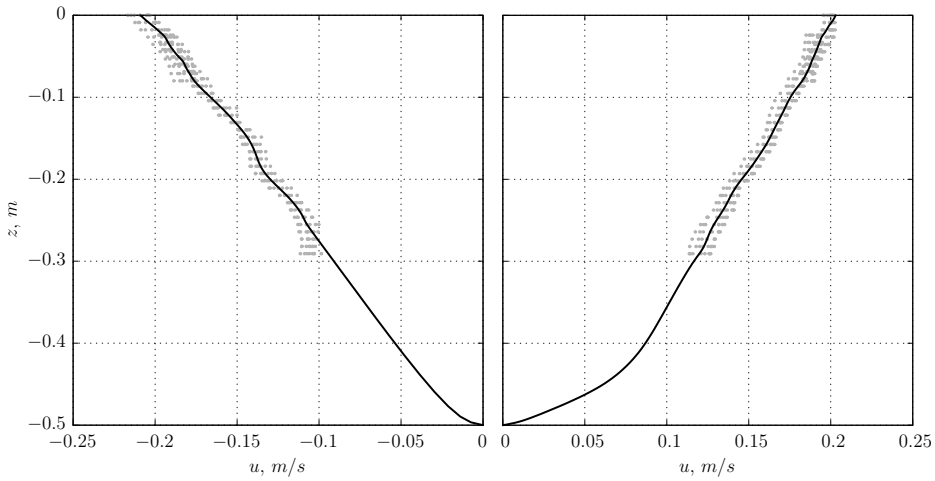

Figure 13: Horizontal velocity profiles for following (left) and opposing (right) currents. PIV measurements (grey dots) and profiles used as the input to the Lagrangian model (solid).

domain with the vertical and horizontal lines of the computational grid. The procedure is illustrated in Figure 12.

We use the numerical wave-current flume to reproduce the results of an experimental study of focused wave groups over sheared currents. The experimental flume is 1.2 m wide and the distance between two piston wavemakers is about 16 m. The depth for all tests is $h = 0.5$ m. A recirculation system with three parallel pumps and vertical inlets 13 m apart is used to create a current. A paddle on the right end of the flume is used as a wave generator and the opposite paddle as an absorber. Trapezoidal wire mesh blocks are installed above the inlet and outlet to condition the flow and create a desired current profile. The surface elevation at selected points along the flume is measured by resistance wave probes and a PIV system is used to measure flow kinematics. An iterative procedure (Buldakov et al., 2017) is used to focus the wave group at a prescribed time and place. We use the same coordinate system as previously with the origin on the water surface at the centre of the flume, the x-axes directed towards the wave generator and the z-axis directed upwards. The wave probe at position $x = 4.7$ m is used to match the linearised amplitude spectrum with the target spectrum, and the wave probe at $x = 0$ for focussing the phase of the generated wave group. A broadband Gaussian spectrum with peak frequency $f_p = 0.6$ Hz is used as the target spectrum. Wave groups having different linearised focus amplitudes A on

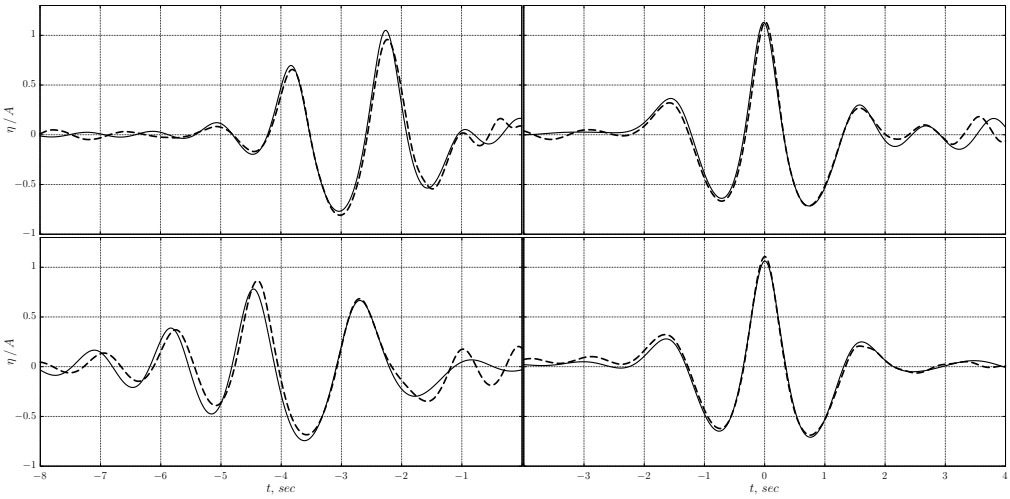

Figure 14: Time history of surface elevation for a wave group at $x = 4.7\,\mathrm{m}$ (left) and $x = 0$ (right) over a following (top) and opposing (bottom) currents. Experiment (dashed) and Lagrangian solver (solid).

opposing and following sheared currents with different surface velocities V_0 are generated in the experimental study. We use a moderately steep wave with $A = 7\,\mathrm{cm}$ propagating on currents with $V_0 \approx 0.2\,\mathrm{m/s}$ as a test case for comparison with numerical results. More details of the experimental setup and methodology can be found in Stagonas et al. (2018a).

Since the experimental and numerical wave flumes have different wave generators and the flow conditioner can not be modelled adequately, direct replication of the experiment in the numerical flume is not possible. We therefore apply in the numerical flume the same iterative wave generation procedure as in the experimental flume using the linearised experimental spectrum as a target. This makes it possible to generate the wave which reproduces the linearised experimental wave with the accuracy of the iterative procedure. This also ensures that the higher order bound wave components are also modelled with the corresponding accuracy. However, the higher order spurious components generated by the experimental and numerical wavemakers are different. This is one of the main sources of difference between experimental and numerical results. The current profiles applied in the Lagrangian model are obtained from PIV measurements of the current velocity, as shown in Figure 13. PIV data only cover the upper part of the water depth ($z > -0.3\,\mathrm{m}$). The shape of the lower part of the profiles is recon-

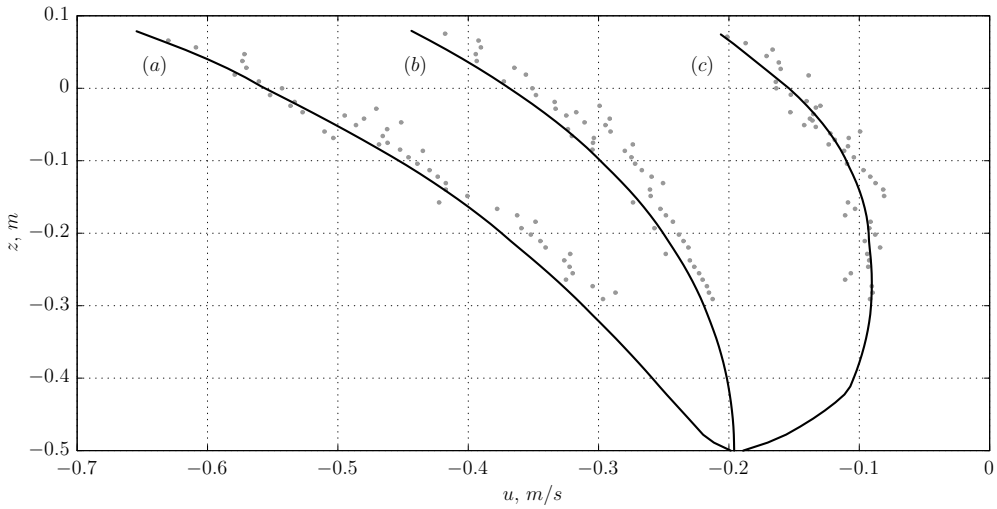

Figure 15: Horizontal velocity profiles under the crest of a focussed wave group over a sheared current. PIV measurements (grey dots) and Lagrangian calculations (solid). (a) – following current; (b) – no current; (c) – opposing current.

structed from the ADV measurements available for currents with a slightly higher discharge.

The comparison of the numerical results with the experiment is shown in Figures 14 and 15. Both the surface elevation (Figure 14) and the combined wave and current velocity profiles (Figure 15) demonstrate good agreement. The contribution of spurious free components to the difference between the measured and calculated surface elevation is clearly visible in Figure 14. For the opposing current, one can also observe the effect of the dispersive error on the phase difference of the results at $x = 4.7\,\mathrm{m}$. Because the wave is focused at the centre of the flume both in the experiment and in the calculations, the dispersive error increases with the increasing distance from the focus position $x = 0$. This error is higher for the opposite current due to the longer effective path of the wave travelling against the current.

6. Concluding remarks

As brief conclusions, we would like to offer reflections on the practical application of wave propagation models to generate incoming waves in wave-structure interaction calculations. It is obvious that the application of a fast but accurate numerical model in a large domain to generate a wave input

for a CFD wave-structure interaction solver operating in a much smaller domain offers considerable savings in computational resources. There are two ways to implement this approach. The first involves modelling a random sea state over a large area and a large period of time. Surface elevation and kinematics of selected events, e.g. extreme waves, is then used as input for a CFD solver. HOS models have a clear advantage for such an approach. The benefits of this method are recognised by the industry. See for example the recent feature article from DNV-GL where an application of a HOS model is reported to provide a realistic nonlinear wave input for the CFD wave-structure interaction code (Bitner-Gregersen, 2017).

In the second approach, a NWT is used in a manner similar to an experimental wave tank for generating a preselected wave event or for replicating a physical wave tank experiment. Any computationally efficient NWT based on an appropriate wave model can be used for this purpose, including the models described in this chapter. None of them seems to have obvious advantages except for the Lagrangian model in the case of waves on sheared currents. For this method, accurate generation of a desired wave event or reconstruction of experimental conditions is important because errors due to incorrect wave input may be larger than errors of a numerical scheme. The application of an iterative wave generation technique may be recommended as an effective solution to this problem. Such techniques are common in wave tank experiments and can be similarly applied in numerical wave tanks (e.g. Fernandez et al., 2014; Buldakov et al., 2017; Stagonas et al., 2018b). An example of an accurate reconstruction of the experimental wave conditions by an advanced iterative technique in a Lagrangian NWT with an application as input to a wave-structure interaction CFD model can be found in Higuera et al. (2018).

The methods described above use the so called one-way coupling between the wave-propagation and CFD models. This means that the wave propagation model is used independently and is not influenced by the CFD model. We believe that for wave-structure interaction problems, this method of communication between models is preferable to real-time two-way coupling, especially when iterative wave generation is used. The computationally demanding CFD component is not executed during the iterative wave generation phase, and the wave propagation component is not executed when the wave interaction with a structure is simulated. Moreover, once generated, wave input can be used in different CFD models using different numerical methods and applied to different structures. One of the technical problems to

be solved when applying the one-way coupling approach is to not allow the waves reflected by the structure to be reflected back to the domain by external domain boundaries. At the same time, the precise transition of the wave kinematics generated by the propagation model to the CFD domain must be ensured. This can be done in different ways.

For example, Higuera et al. (2018) used Lagrangian kinematics and surface elevation to specify the boundary condition for velocity on a front boundary of a rectangular CFD domain. Active dissipation was applied at the rear boundary and passive dissipation at the side boundaries of the domain. Another approach is using a cylindrical grid with a ring-shaped relaxation zone. This mesh type provides better resolution around a structure. The equations within the relaxation zone are modified to introduce a dissipation of disturbances of the incoming wave solution with a dissipation coefficient gradually increasing from zero on the inner edge of the relaxation zone to a high value on its outer edge. In this way, the incoming wave is implemented on an outer boundary of the computational domain and propagates freely into the domain interior. At the same time, the waves reflected by the structure propagates freely in the field and dissipates inside the relaxation zone without being reflected back. The size of the computational domain is proportional to the wavelength of the incoming wave and the width of the relaxation zone to the length of the wave reflected or radiated by the structure. Normally, the reflected wave has the same length as the incoming wave, but in certain situations, e.g. for slender structures, the peak of the reflected spectrum is shifted towards higher frequencies. For such structures the width of the relaxation zone can be reduced. This is also the case for waves radiated by ringing structures. The optimal sizes of the main computation domain and the relaxation zone depend on a particular wave and structure. Practical recommendations on their selection for different types of structures and waves should be developed as a result of the convergence study with respect to these parameters.

Acknowledgments

The work on wave over sheared currents presented in this chapter is supported by EPSRC within the Supergen Marine Technology Challenge (Grant EP/J010316/1). The author also thanks Dr. Dimitris Stagonas for performing experiments on wave propagation over current used in this work and for analysis of experimental data.

References

Bateman, W., Swan, C., Taylor, P., 2001. On the efficient numerical simulation of directionally spread surface water waves. Journal of Computational Physics 174 (1), 277 – 305.

Bitner-Gregersen, E., May 2017. Hacking wave structure. Next generation wave-structure interaction codes. Feature article, DNV-GL.

Bonnefoy, F., Ducrozet, G., Touzé, D. L., Ferrant, P., 2010. Time domain simulation of nonlinear water waves using spectral methods. In: Ma, Q. (Ed.), Advances in Numerical Simulation of Nonlinear Water Waves. World Scientific, Ch. 4, pp. 129–164.

Braess, H., Wriggers, P., 2000. Arbitrary Lagrangian Eulerian finite element analysis of free surface flow. Computational Methods in Applied Mechhanics and Engineering 190, 95–109.

Brennen, C., Whitney, A. K., 1970. Unsteady, free surface flows; solutions employing the Lagrangian description of the motion. In: 8th Symposium on Naval Hydrodynamics. Office of Naval Research, pp. 117–145.

Buldakov, E., 2013. Tsunami generation by paddle motion and its interaction with a beach: Lagrangian modelling and experiment. Coastal Engineering 80, 83–94.

Buldakov, E., 2014. Lagrangian modelling of fluid sloshing in moving tanks. Journal of Fluids and Structures 45, 1–14.

Buldakov, E., Higuera, P., Stagonas, D., 2019. Numerical models for evolution of extreme wave groups. submitted to Applied Ocean Research.

Buldakov, E., Stagonas, D., Simons, R., 2015. Langrangian numerical wave-current flume. In: Proceedings of 30th International Workshop on Water Waves and Floating Bodies. Bristol, UK, pp. 25–28.

Buldakov, E., Stagonas, D., Simons, R., 2017. Extreme wave groups in a wave flume: Controlled generation and breaking onset. Coastal Engineering 128, 75 – 83.

Cai, X., Langtangen, H., Nielsen, B., Tveito, A., 1998. A finite element method for fully nonlinear water waves. Journal of Computational Physics 143 (2), 544–568.

Chan, R. K.-C., 1975. A generalized arbitrary Lagrangian-Eulerian method for incompressible flows with sharp interfaces. Journal of Computational Physics 17, 311–331.

Chen, L., Stagonas, D., Santo, H., Buldakov, E., Simons, R., Taylor, P., Zang, J., 2019. Numerical modelling of interactions of waves and sheared currents with a surface piercing vertical cylinder. Coastal Engineering 145, 65–83.

Chen, L.-F., Ning, D.-Z., Teng, B., Zhao, M., 2017. Numerical and experimental investigation of nonlinear wave-current propagation over a submerged breakwater. Journal of Engineering Mechanics 143 (9), 04017061–1 – 04017061–14.

Craig, W., Sulem, C., 1993. Numerical simulation of gravity waves. Journal of Computational Physics 108 (1), 73 – 83.

Da Silva, A., Peregrine, D., 1988. Steep, steady surface waves on water of finite depth with constant vorticity. Journal of Fluid Mechanics 195, 281–302.

Dias, F., Bridges, T. J., 2006. The numerical computation of freely propagating time-dependent irrotational water waves. Fluid Dynamics Research 38 (12), 803–830.

Dommermuth, D., Yue, D., 1987a. A high-order spectral method for the study of nonlinear gravity waves. Journal of Fluid Mechanics 184, 267–288.

Dommermuth, D., Yue, D., 1987b. Numerical simulations of nonlinear axisymmetric flows with a free surface. Journal of Fluid Mechanics 178, 195–219.

Dommermuth, D., Yue, D., Lin, W., Rapp, R., 1988. Deep-water plunging breakers: A comparison between potential theory and experiments. Journal of Fluid Mechanics 189, 423–442.

Ducrozet, G., Bingham, H. B., Engsig-Karup, A. P., Bonnefoy, F., Ferrant, P., 2012a. A comparative study of two fast nonlinear freesurface water wave models. International Journal for Numerical Methods in Fluids 69 (11), 1818–1834.

Ducrozet, G., Bonnefoy, F., Le Touzé, D., Ferrant, P., 2007. 3-D HOS simulations of extreme waves in open seas. Natural Hazards and Earth System Science 7 (1), 109–122.

Ducrozet, G., Bonnefoy, F., Le Touzé, D., Ferrant, P., 2012b. A modified High-Order Spectral method for wavemaker modeling in a numerical wave tank. European Journal of Mechanics - B/Fluids 34, 19 – 34.

Eatock Taylor, R., Wu, G., Bai, W., Hu, Z., 2008. Numerical wave tanks based on finite element and boundary element modeling. Journal of Offshore Mechanics and Arctic Engineering 130 (3), 031001–1 – 031001–8.

Engsig-Karup, A., Eskilsson, C., Bigoni, D., 2016. A stabilised nodal spectral element method for fully nonlinear water waves. Journal of Computational Physics 318, 1 – 21.

Fenton, J., Rienecker, M., 1982. A Fourier method for solving nonlinear water-wave problems: Application to solitary-wave interactions. Journal of Fluid Mechanics 118, 411–443.

Fenton, J. D., 1999. Numerical methods for nonlinear waves. In: Liu, P. L. F. (Ed.), Advances in Coastal and Ocean Engineering. Vol. 5. World Scientific, pp. 241–324.

Fernandez, H., Sriram, V., Schimmels, S., Oumeraci, H., 2014. Extreme wave generation using self correcting method – revisited. Coastal Engineering 93, 15–31.

Fochesato, C., Dias, F., 2006. A fast method for nonlinear three-dimensional free-surface waves. Proceedings of the Royal Society of London A: Mathematical, Physical and Engineering Sciences 462 (2073), 2715–2735.

Fochesato, C., Grilli, S., Dias, F., 2007. Numerical modeling of extreme rogue waves generated by directional energy focusing. Wave Motion 44 (5), 395 – 416.

Fritts, M., Boris, J., 1979. The Lagrangian solution of transient problems in hydrodynamics using a triangular mesh. Journal of Computational Physics 31 (2), 173–215.

Gomez-Gesteira, M., Rogers, B. D., Dalrymple, R. A., Crespo, A. J., 2010. State-of-the-art of classical SPH for free-surface flows. Journal of Hydraulic Research 48 (sup1), 6–27.

Gouin, M., Ducrozet, G., Ferrant, P., 2016. Development and validation of a non-linear spectral model for water waves over variable depth. European Journal of Mechanics - B/Fluids 57, 115 – 128.

Grilli, S., Guyenne, P., Dias, F., 2001. A fully non-linear model for three-dimensional overturning waves over an arbitrary bottom. International Journal for Numerical Methods in Fluids 35 (7), 829–867.

Grilli, S., Skourup, J., Svendsen, I., 1989. An efficient boundary element method for nonlinear water waves. Engineering Analysis with Boundary Elements 6 (2), 97–107.

Grilli, S., Svendsen, I., 1990. Corner problems and global accuracy in the boundary element solution of nonlinear wave flows. Engineering Analysis with Boundary Elements 7 (4), 178 – 195.

Grilli, S. T., Dias, F., Guyenne, P., Fochesato, C., Enet, F., 2010. Progress in fully nonlinear potential flow modeling of 3D extreme ocean waves. In: Ma, Q. (Ed.), Advances in Numerical Simulation of Nonlinear Water Waves. World Scientific, Ch. 3, pp. 75–128.

Guignard, S., Grilli, S., 2001. Modeling of wave shoaling in a 2D-NWT using a spilling breaker model. In: Proceedings of the Eleventh International Offshore and Polar Engineering Conference. Vol. 3. Stavanger, Norway, pp. 116–123.

Guo, L.-D., Sun, D.-P., Wu, H., 2012. A new numerical wave flume combining the 0-1 type BEM and the VOF method. Journal of Hydrodynamics, Ser. B 24 (4), 506–517.

Haussling, H., Coleman, R., 1979. Nonlinear water waves generated by an accelerated circular cylinder. Journal of Fluid Mechanics 92 (4), 767–781.

Herivel, J. W., 1955. The derivation of the equations of motion of an ideal fluid by Hamilton's principle. Proc. Cambridge Philos. Soc. 51, 344–349.

Higuera, P., Buldakov, E., Stagonas, D., 2018. Numerical modelling of wave interaction with a FSPO using a combination of OpenFOAM and Lagrangian models. In: Proceedings of the Twenty Eighth International Offshore and Polar Engineering Conference. Sapporo, Japan, pp. 1486–1491.

Hirt, C., Cook, J., Butler, T., 1970. A Lagrangian method for calculating the dynamics of an incompressible fluid with free surface. Journal of Computational Physics 5 (1), 103–124.

Isaacson, M., 1982. Nonlinear-wave effects on fixed and floating bodies. Journal of Fluid Mechanics 120, 267–281.

Jiang, S.-C., Teng, B., Gou, Y., Ning, D.-Z., 2012. A precorrected-fft higher-order boundary element method for wavebody problems. Engineering Analysis with Boundary Elements 36 (3), 404–415.

Kawahara, M., Anjyu, A., 1988. Lagrangian finite element method for solitary wave propagation. Computational Mechanics 3 (5), 299–307.

Keller, H. B., 1971. A new difference scheme for parabolic problems. In: Numerical Solution of Partial Differential Equations, II (SYNSPADE 1970) (Proc. Sympos., Univ. of Maryland, College Park, Md., 1970). Academic Press, New York, pp. 327–350.

Kim, C., Clément, A., Tanizawa, K., 1999. Recent research and development of numerical wave tanks - a review. International Journal of Offshore and Polar Engineering 9 (4), 241–256.

Kim, S.-H., Yamashiro, M., Yoshida, A., 2010. A simple two-way coupling method of BEM and VOF model for random wave calculations. Coastal Engineering 57 (11), 1018–1028.

Lachaume, C., Biausser, B., Grilli, S., Frauni, P., Guignard, S., 25-30 May 2003. Modeling of breaking and post-breaking waves on slopes by coupling of BEM and VOF methods. In: Proceedings of the Thirteenth International Offshore and Polar Engineering Conference. Honolulu, Hawaii, USA, pp. 1698–1704.

Lamb, H., 1932. Hydrodynamics. Cambridge University Press.

Landrini, M., Colagrossi, A., Greco, M., Tulin, M., 2012. The fluid mechanics of splashing bow waves on ships: A hybrid BEM-SPH analysis. Ocean Engineering 53, 111–127.

Lin, P., 2008. Numerical modeling of water waves. Taylor & Francis, London.

Longuet-Higgins, M. S., Cokelet, E. D., 1976. The deformation of steep surface waves on water. I. A numerical method of computation. Proceedings of the Royal Society of London A: Mathematical, Physical and Engineering Sciences 350 (1660), 1–26.

Ma, Q. (Ed.), 2010. Advances in numerical simulation of nonlinear water waves. Vol. 11 of Advances in Coastal and Ocean Engineering. World Scientific.

Ma, Q., Yan, S., 2006. Quasi ALE finite element method for nonlinear water waves. Journal of Computational Physics 212 (1), 52 – 72.

Ma, Q. W., Wu, G. X., Eatock Taylor, R., 2001. Finite element simulation of fully nonlinear interaction between vertical cylinders and steep waves. Part 1: methodology and numerical procedure. International Journal for Numerical Methods in Fluids 36 (3), 265–285.

Ma, Q. W., Yan, S., 2010. QALE-FEM method and its application to the simulation of free-responses of floating bodies and overturning waves. In: Ma, Q. (Ed.), Advances in Numerical Simulation of Nonlinear Water Waves. World Scientific, Ch. 5, pp. 165–202.

NAG, 2016. NAG Library Manual, Mark 26. The Numerical Algorithms Group Ltd, Oxford, UK.

New, A., McIver, P., Peregrine, D., 1985. Computations of overturning waves. Journal of Fluid Mechanics 150, 233–251.

Nimmala, S., Yim, S., Grilli, S., 2013. An efficient three-dimensional FNPF numerical wave tank for large-scale wave basin experiment simulation. Journal of Offshore Mechanics and Arctic Engineering 135 (2), 021104–1 – 021104–10.

Ning, D., Zang, J., Liu, S., Eatock Taylor, R., Teng, B., Taylor, P., 2009. Free-surface evolution and wave kinematics for nonlinear uni-directional focused wave groups. Ocean Engineering 36 (15), 1226 – 1243.

Nishimura, H., Takewaka, S., 1988. Numerical analysis of two-dimensional wave motion using Lagrangian description. Doboku Gakkai Rombun-Hokokushu/Proceedings of the Japan Society of Civil Engineers 9 (5), 1910–199, in Japanese.

Ohyama, T., Nadaoka, K., 1991. Development of a numerical wave tank for analysis of nonlinear and irregular wave field. Fluid Dynamics Research 8 (5–6), 231–251.

Ölmez, H., Milgram, J., 1995. Numerical methods for nonlinear interactions between water waves. Journal of Computational Physics 118 (1), 62 – 72.

Radovitzky, R., Ortiz, M., 1998. Lagrangian finite element analysis of newtonian fluid flows. International Journal for Numerical Methods in Engineering 43 (4), 607–619.

Ramaswamy, B., Kawahara, M., 1987. Lagrangian finite element analysis applied to viscous free surface fluid flow. International Journal for Numerical Methods in Fluids 7 (9), 953–984.

Robertson, I., Sherwin, S., 1999. Free-surface flow simulation using hp/spectral elements. Journal of Computational Physics 155 (1), 26 – 53.

Ryu, S., Kim, M. H., Lynett, P. J., 2003. Fully nonlinear wave-current interactions and kinematics by a BEM-based numerical wave tank. Computational Mechanics 32 (4), 336–346.

Schäffer, H. A., 2008. Comparison of Dirichlet-Neumann operator expansions for nonlinear surface gravity waves. Coastal Engineering 55 (4), 288 – 294.

Seiffert, B. R., Ducrozet, G., 2018. Simulation of breaking waves using the high-order spectral method with laboratory experiments: wave-breaking energy dissipation. Ocean Dynamics 68 (1), 65–89.

Seiffert, B. R., Ducrozet, G., Bonnefoy, F., 2017. Simulation of breaking waves using the high-order spectral method with laboratory experiments: Wave-breaking onset. Ocean Modelling 119, 94 – 104.

Sharma, G., Agarwala, A., Bhattacharya, B., 2013. A fast parallel Gauss Jordan algorithm for matrix inversion using CUDA. Computers & Structures 128, 31–37.

Skyner, D., 1996. A comparison of numerical predictions and experimental measurements of the internal kinematics of a deep-water plunging wave. Journal of Fluid Mechanics 315, 51–64.

Souli, M., Benson, D. J., 2013. Arbitrary Lagrangian Eulerian and Fluid-Structure Interaction: Numerical Simulation. Wiley-ISTE.

Sriram, V., Ma, Q., Schlurmann, T., 2014. A hybrid method for modelling two dimensional non-breaking and breaking waves. Journal of Computational Physics 272, 429–454.

Stagonas, D., Buldakov, E., Simons, R., 2018a. Experimental generation of focusing wave groups on following and adverse-sheared currents in a wave-current flume. Journal of Hydraulic Engineering 144 (5), 04018016–1 – 04018016–11.

Stagonas, D., Higuera, P., Buldakov, E., 2018b. Simulating breaking focused waves in CFD: Methodology for controlled generation of first and second order. Journal of Waterway, Port, Coastal and Ocean Engineering 144 (2), 06017004–1 – 06017004–8.

Staroszczyk, R., 2009. A Lagrangian finite element analysis of gravity waves in water of variable depth. Archives of Hydroengineering and Environmental Mechanics 56 (1–2), 43–61.

Subramani, A., Beck, R., Schultz, W., 1998. Suppression of wave breaking in nonlinear water wave computations. In: Proceedings of 13th International Workshop on Water Waves and Floating Bodies. Alphen aan den Rijn, The Netherlands, pp. 139–142.

Tian, Z., Perlin, M., Choi, W., 2012. An eddy viscosity model for two-dimensional breaking waves and its validation with laboratory experiments. Physics of Fluids 24 (3), 036601–1 – 036601–23.

Tsai, W., Yue, D. K. P., 1996. Computation of nonlinear free-surface flows. Annual Review of Fluid Mechanics 28, 249–278.

Vinje, T., Brevig, P., 1981. Numerical simulation of breaking waves. Advances in Water Resources 4 (2), 77 – 82.

Violeau, D., Rogers, B. D., 2016. Smoothed particle hydrodynamics (SPH) for free-surface flows: past, present and future. Journal of Hydraulic Research 54 (1), 1–26.

Wang, C., Wu, G., 2011. A brief summary of finite element method applications to nonlinear wave-structure interactions. Journal of Marine Science and Application 10 (2), 127–138.

Wang, P., Yao, Y., Tulin, M. P., 1995. An efficient numerical tank for nonlinear water waves, based on the multi-subdomain approach with BEM. International Journal for Numerical Methods in Fluids 20 (12), 1315–1336.

West, B. J., Brueckner, K. A., Janda, R. S., Milder, D. M., Milton, R. L., 1987. A new numerical method for surface hydrodynamics. Journal of Geophysical Research: Oceans 92 (C11), 11803–11824.

Wu, G., Eatock Taylor, R., 1994. Finite element analysis of two-dimensional non-linear transient water waves. Applied Ocean Research 16 (6), 363 – 372.

Wu, G., Eatock Taylor, R., 1995. Time stepping solutions of the two-dimensional nonlinear wave radiation problem. Ocean Engineering 22 (8), 785 – 798.

Wu, G., Eatock Taylor, R., 2003. The coupled finite element and boundary element analysis of nonlinear interactions between waves and bodies. Ocean Engineering 30 (3), 387 – 400.

Wu, G. X., Hu, Z. Z., 2004. Simulation of nonlinear interactions between waves and floating bodies through a finite-element-based numerical tank. Proceedings of the Royal Society of London A: Mathematical, Physical and Engineering Sciences 460 (2050), 2797–2817.

Xue, M., Xü, H., Liu, Y., Yue, D., 2001. Computations of fully nonlinear three-dimensional wave-wave and wave-body interactions. Part 1 .Dynamics of steep three-dimensional waves. Journal of Fluid Mechanics 438, 11–39.

Yan, H., Liu, Y., 2011. An efficient high-order boundary element method for nonlinear wavewave and wave-body interactions. Journal of Computational Physics 230 (2), 402 – 424.

Yan, S., Ma, Q. W., 2010. QALE-FEM for modelling 3D overturning waves. International Journal for Numerical Methods in Fluids 63 (6), 743–768.

Zienkiewicz, O., Taylor, R., Nithiarasu, P., 2005. Finite Element Method for Fluid Dynamics, 6th Edition. Elsevier.